Journal of Nanobiotechnology

RESEARCH

Open Access

NIR-responsive $Cu_{2-x}Se$@Fc nanoparticles for photothermal- ferroptosis combination therapy in esophageal cancer

Linlin Shi[1†], Ying Yu[1†], Jiayi Li[1], Beng Ma[3], Xiaoman Zhang[1], Pingjuan Yang[1], Pan Chen[1], Zhifeng Qu[1], Fengqi Zhang[1], Ke Liu[1], Shegan Gao[1,2*] and Haoyan Cheng[3*]

Abstract

Esophageal cancer (EC) represents a highly recurrent and aggressive malignancy within the digestive system. However, conventional therapeutic strategies exhibit notable limitations in their clinical applications. Photothermal therapy (PTT), combined with ferroptosis, has attracted considerable attentions, emerging as a promising novel strategy for EC treatment. Therefore, there is a critical need to develop a drug delivery system capable of effectively integrating these two therapeutic approaches. In this work, we report a novel drug delivery system based on ferrocene (Fc), which is mixed with lauric acid (a phase-change material with a melting point around 44 °C) and then coated on the surface of $Cu_{2-x}Se$ nanoparticles. The photothermal properties of $Cu_{2-x}Se$ triggers the melting of lauric acid under near-infrared (NIR) laser irradiation, facilitating controlled release of Fc. Following internalization by tumor cells via endocytosis, the synergistic effect of PTT and ferroptosis, triggered by $Cu_{2-x}Se$@Fc, induced immunogenic cell death, which promoted dendritic cell maturation and cytotoxic T lymphocytes recruitment while decreasing the proportion of regulatory T cells, thereby strengthening the antitumor immune surveillance and improving the therapeutic efficacy of Anti-PD-1 blockade. These findings propose that the NIR-responsive $Cu_{2-x}Se$@Fc formulation represents a promising and effective strategy with prospecting application for cancer treatment.

Keywords Esophageal cancer, Photothermal therapy, Ferroptosis, $Cu_{2-x}Se$@Fc nanoparticle

Introduction

Currently, the main clinical approach for treating esophageal cancer (EC) involves a combination of surgery and neoadjuvant chemoradiotherapy. However, this treatment is associated with considerable adverse effects, and the overall rates of recurrence and progression remain elevated, with the 5-year cancer-specific survival rate remaining below 20% [1-3]. Therefore, there is an urgent need to enhance treatment outcomes and minimize the toxic effects.

In the field of therapeutic interventions, neotype treatment modalities aimed at extending patient survival rates and enhancing quality of life are being explored

†Linlin Shi and Ying Yu contributed equally to this work.

*Correspondence:
Shegan Gao
gsg112258@163.com
Haoyan Cheng
chenghaoyan@haust.edu.cn

Full list of author information is available at the end of the article

Graphical abstract

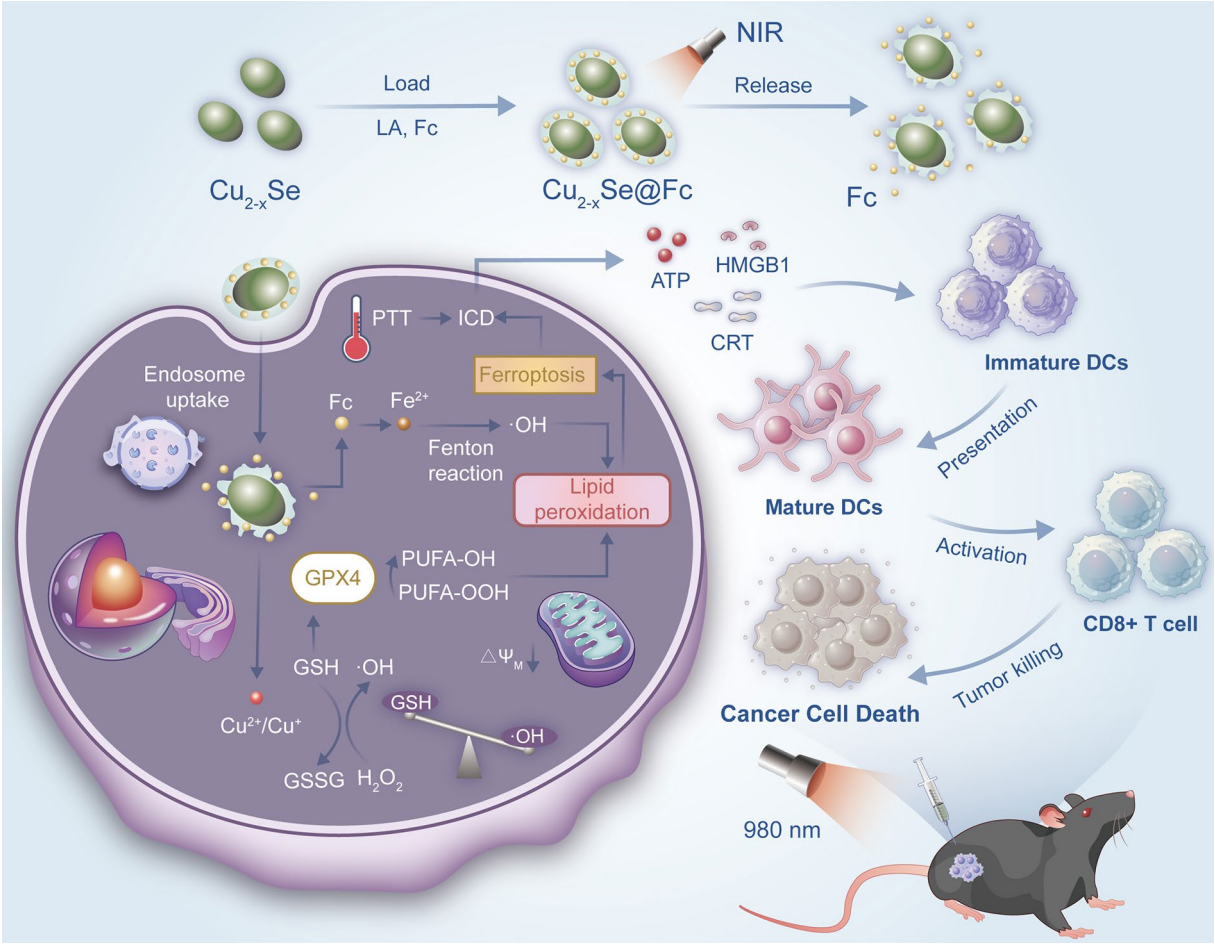

and innovated. Given its nature as a superficial tumor with direct access via the esophageal channel, EC presents a promising target for near-infrared (NIR)-induced photothermal therapy (PTT) [4]. The efficacy of PTT depends on the efficient conversion of light to heat by photothermal agents (PTA) [5, 6]. Recent investigations have focused on plasma-doped semiconducting nanoparticles (NPs), specifically copper chalcogenides, for their photothermal conversion capabilities [7]. These NPs exhibit localized surface plasmon resonance (LSPR) effects NIR wavelengths, thereby enabling effective photothermal conversion across a broad electromagnetic spectrum [8]. Nevertheless, the efficacy of PTT in treating solid tumors is hindered by the intricate physiological and pathological barriers within the tumor microenvironment (TME), restricting light penetration depth and impeding the adequate accumulation and distribution of photothermal materials at the local tumor site [9]. Additionally, the uncontrollable diffusion of thermal energy may pose a risk to adjacent tissues. Mild photothermal therapy (MPTT) has emerged as a strategy to address these challenges, exhibiting excellent performance in tumor therapy [10]. Research has demonstrated that mild heat exposure can notably decrease the production of antioxidants and disrupt the redox balance within the tumor [11]. However, PTT alone may not achieve complete tumor ablation and often requires combination with other treatment strategies [12-14].

Ferroptosis, a regulated cell death mechanism distinct from apoptosis and autophagy, is primarily driven by the accumulation of reactive oxygen species (ROS) catalyzed by Fe^{2+} through the Fenton reaction, resulting in the production of lethal levels of lipid peroxides (LPO) [15]. Subsequently, glutathione (GSH) depletion results in the decreased activity of glutathione peroxidase 4 (GPX4) and the inability of LPO to be metabolized through the GPX4-catalyzed reduction reaction [16]. The exploration of ferroptosis as a target for tumor therapy presents a multitude of possibilities for advancing clinical oncology through novel approaches and diagnostic strategies

[17]. The synergistic combination of MPTT with ferroptosis has the potential to augment tumor cytotoxicity significantly. Elevating the temperature in the presence of PTA was reported to dramatically accelerate the Fenton reaction, allowing the combination of PTT with ferroptosis of the tumor [18, 19]. Notably, such synergy induces immunogenic cell death (ICD) to stimulate dendritic cell (DC) maturation and enhance the recruitment of cytotoxic T lymphocytes (CTLs) toward tumor site, activating adaptive immune responses toward solid tumors [20, 21]. The fundamental principle of ferroptosis induced by NPs involves introducing a substantial quantity of Fe^{2+} and the perturbation of cellular redox equilibrium [22]. Nonetheless, the utilization of crystalline iron necessitates acidification for gradual release, whereas Fe^{2+} is prone to oxidation during preparation and storage [23, 24]. Therefore, an integrated system with photothermal properties and Fe^{2+} activation capacity was selected for photothermal-ferroptosis combination therapy.

Herein, we present a facile and versatile strategy for the effective eradication of EC by combining photothermal and chemo therapies through the use of $Cu_{2-x}Se$ (CS) NPs and ferrocene (Fc), a small molecule inducer of ferroptosis. The $Cu_{2-x}Se$ itself can serve as a photothermal transducer capable of absorbing NIR light and then converting the light into heat with high efficiency. We use a phase-change material lauric acid (LA) as the medium to help load Fc. When exposed to the NIR laser, the temperature increased to melt LA (above 44 ℃), the Fc loaded could release in a controllable fashion [25-28]. Furthermore, Cu^{2+} in $Cu_{2-x}Se$ can be converted to Cu^{+} by reduced GSH, which then reacts with H_2O_2 to produce hydroxyl radicals (·OH) and Cu^{2+} via a Fenton-like reaction, driving a destructive peroxidation cascade reaction [29, 30]. The NIR laser activation approach initiated the therapeutic process selectively within tumor tissues, leading to simultaneous high efficacy in photothermal-ferroptosis tumor therapy while causing minimal damage to normal tissues.

Results and discussion

Preparation and characterization of CS@Fc

Scheme 1 indicates the schematic procedure for loading of LA and Fc and the controlled release of Fc at the tumor site. The CS NPs with an average size of 62.63 nm (Fig. S1 and 1 A-B) were prepared according to previously reported literature [31]. The high-resolution transmission electron microscopy (HRTEM) image in Fig. 1C revealed a lattice spacing of 0.318 nm, corresponding to the (111) crystal plane of cubic phase CS. The X-ray diffraction (XRD) spectrum in Fig. 1D further confirmed the cubic phase of the prepared CS NPs. Elemental mapping results indicated a homogeneous distribution of Se and Cu within the NPs (Fig. 1E). X-ray photoelectron spectroscopy (XPS) analysis confirmed the presence of Cu, Fe, and Se in CS@Fc ($Cu_{2-x}Se$@Fc), demonstrating the successful loading of Fc (Fig. 1F). The peaks at 931.97 and 951.68 eV in the high-resolution Cu 2p XPS spectra corresponds to Cu^{+}, while peaks at 934.28 and 954.08 eV were associated with Cu^{2+} (Fig. S2). The Fc was loaded onto the surface of CS through LA to obtain CS@Fc NPs. Transmission electron microscopy (TEM) revealed the successful encapsulation of LA, with a thickness of approximately 6.20 nm (Fig. 1G-H). Furthermore, under 37 °C conditions, dynamic light scattering (DLS) was used to monitor the hydrodynamic diameter of CS@Fc over seven days. The results revealed no significant changes in the hydration particle size in PBS, RPMI-1640, or RPMI-1640 supplemented with 10% fetal bovine serum (FBS) (Fig. 1I). Furthermore, continuous UV-Vis absorption spectroscopy monitoring of the CS@Fc suspension in RPMI-1640 over 72 h showed negligible variations in the absorption spectra (Fig. S3). These findings confirm the excellent stability of CS@Fc nanoparticles under physiological conditions. In comparison, under simulated TME conditions (pH 6.4), CS@Fc NPs exhibit significant degradation properties (Fig. S4). This degradation characteristic is advantageous as it potentially mitigates the toxicity of CS@Fc NPs within biological systems.

The photothermal capacity of CS@Fc

As displayed in Fig. 2A, the UV-vis spectra of CS and CS@Fc NPs showed peaks around 980, which is a favorable wavelength range for deep tissue light penetration. The photothermal performance of CS@Fc NPs was displayed in Fig. 2B-C. Under 980 nm NIR laser irradiation at 1.0 W/cm^2, the temperature increased rapidly, suggesting that the CS maintained remarkable photothermal properties after encapsulation of the LA and Fc on the surface. The escalation in temperature is intricately associated with the power density of the laser and the concentration of CS@Fc. Infrared thermal images showed rapid heating of CS@Fc suspension to elevated temperatures within 5 min of NIR exposure (Fig. 2D). Based on the temperature change curves of CS@Fc suspension and H_2O (Fig. 2E), utilizing the relevant equation, the photothermal conversion efficiency of CS@Fc was determined to be 70.58% (Fig. 2F), which is significantly higher than that of conventional materials, such as Au nanorods [32, 33]. Repeated heating and cooling cycles under NIR irradiation demonstrated the excellent photothermal stability of the CS@Fc NPs (Fig. 2G).

In vitro Fc release

To quantify the loading capacity of Fc in CS@Fc, Fc solutions with varying concentrations were prepared, and a linear relationship between Fc concentration and UV

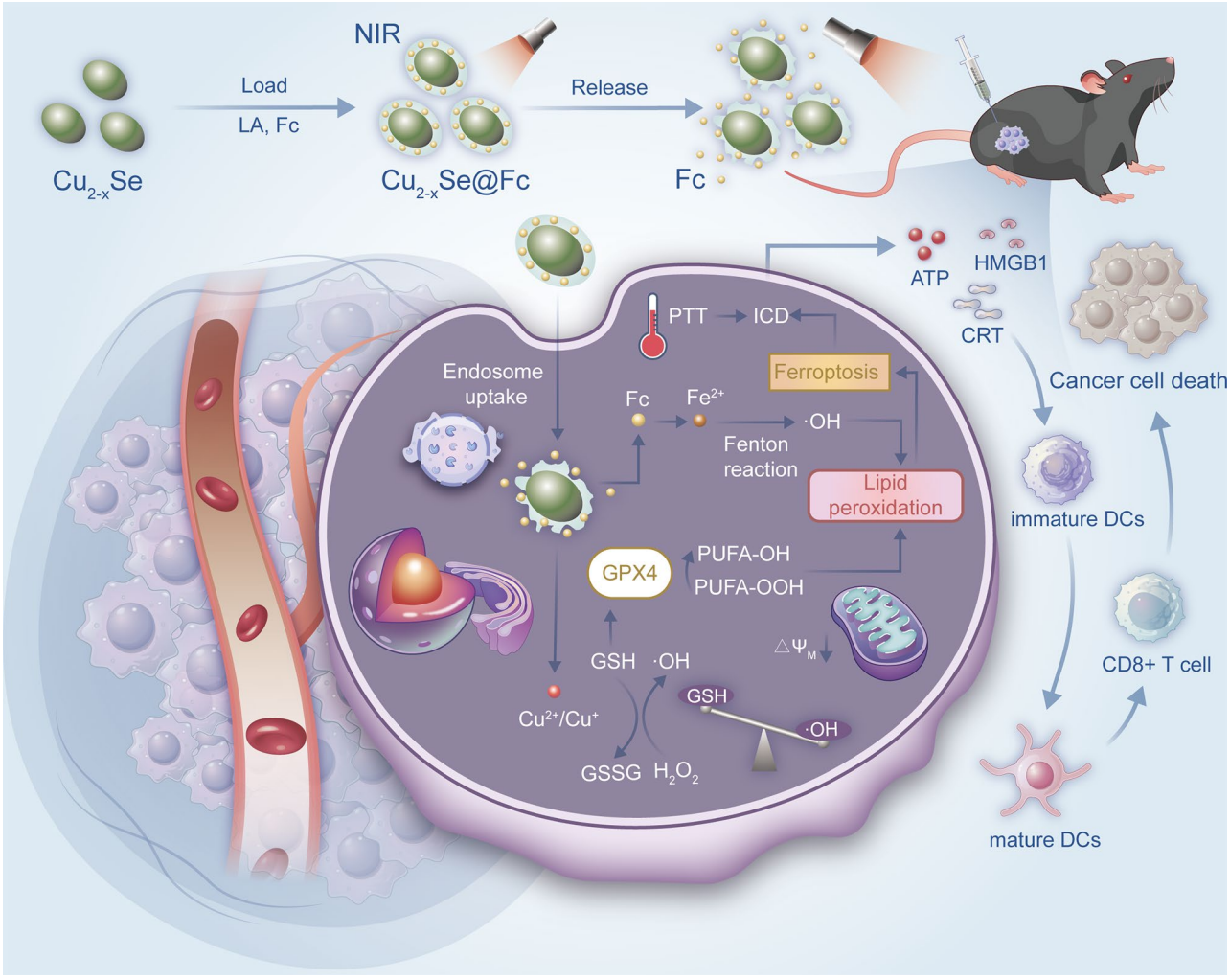

Scheme 1 Illustration of a photothermal-ferroptosis combination therapy mediated by CS@Fc

absorbance at 441 nm was established (Fig. S5). After centrifugation to remove the supernatant, the CS@Fc NPs were dispersed in dimethylformamide (DMF) to fully release the loaded Fc. The Fc concentration in the supernatant was measured using the established calibration curve, yielding a Fc loading of 152.23 μg/mL. The release kinetics of Fc from the CS@Fc NPs were further investigated at 45 °C, which resulted in a rapid Fc release, reaching 129.5 μg/mL within 5 min (Fig. 2H-I).

In vitro cytotoxicity of CS@Fc

Cell viability was detected to assess the cytotoxicity of CS@Fc against KYSE70 cells (Fig. 3A). In the absence of NIR laser irradiation, various concentrations of CS@Fc treatment exhibited low cytotoxicity. Furthermore, there were no significant differences in cell viability across the groups, a trend similar to that observed in HUVEC (Fig. S6), indicating the excellent biocompatibility of CS@Fc. However, upon NIR laser irradiation, the viability of KYSE70 cells decreased significantly with increasing CS@Fc concentrations. Following various treatments, the survival rates of the cells subjected to CS and CS@Fc combined irradiation were 54.47% and 50.61% respectively, both of which significantly lower than those observed in the non-irradiated group, corroborating the photothermal cytotoxicity of CS and CS@Fc (Fig. 3B). To further evaluate cellular membrane damage, the release of lactate dehydrogenase (LDH) was quantified. The results (Fig. 3C) demonstrated that KYSE70 cells incubated with CS@Fc indicated a marked increase in LDH release upon NIR laser exposure. This rate was approximately 7-times than that of the cells in the PBS group and 4-times than that of CS-treated cells exposed to NIR laser. These findings suggested that the combination of CS@Fc and NIR laser irradiation displayed a heightened propensity for membrane disruption compared to photothermal effects alone.

The intracellular localization of CS@Fc was further investigated using confocal laser scanning microscopy (CLSM). CS@DiD was prepared and incubated with

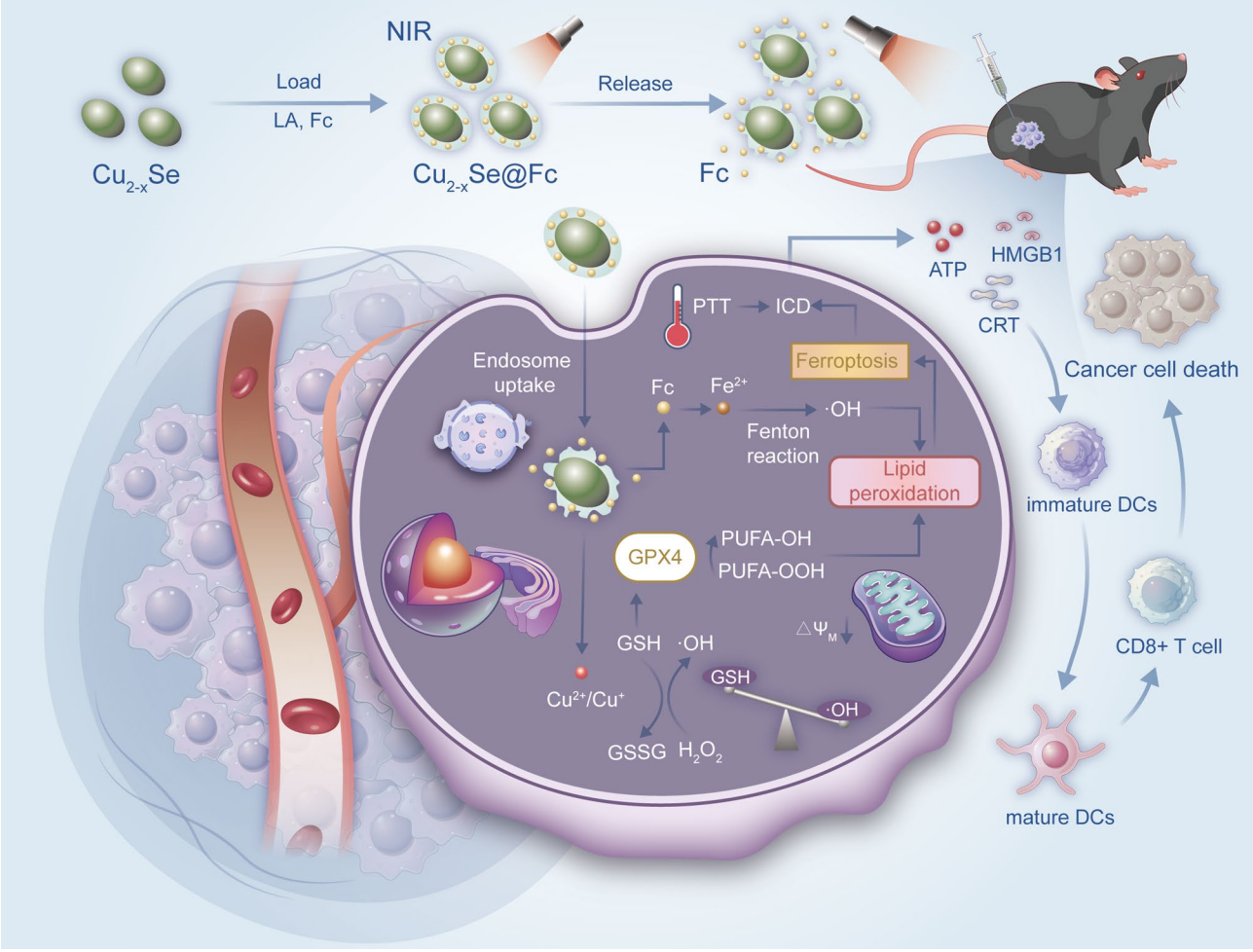

Fig. 1 (**A**) TEM image of the CS NPs. Scale bar: 50 nm. (**B**) The size distributions of the CS NPs. (**C**) HRTEM image of the CS NPs. Scale bar: 5 nm. The illustration in (**C**). Scale bar: 2 nm. (**D**) XRD pattern of CS. (**E**) Elemental mapping of the CS NPs. Scale bar: 30 nm. (**F**) XPS survey spectrum of CS@Fc. (**G**) TEM image of the CS@Fc NPs. Scale bar: 50 nm. (**H**) The thickness of LA on the surface of the CS NPs. (**I**) The hydrodynamic sizes of CS@Fc NPs dispersed in PBS, RPMI-1640, and 10% FBS-containing RPMI-1640 over 7 days

KYSE70 cells to evaluate cellular uptake, and the fluorescence intensity of DiD was monitored at different time points. The colocalization assay showed that most DiD molecules were localized in lysosomes within 6 h, indicating rapid cellular internalization of CS@DiD (Fig. 3D).

Subsequently, as shown in the fluorescence images of Calcein-AM/PI staining (Fig. 3E), the CS and CS@Fc treatments triggered cell death in the presence of the NIR laser compared to non-irradiated groups. This observation suggested that the combined therapy resulted in more significant damage to KYSE70 cells. Meanwhile, flow cytometry revealed that the apoptotic cell proportion in the CS + NIR group was 38.03%, whereas the cell apoptosis rate reached 49.93% in the CS@Fc + NIR group, illustrating effective induction of apoptosis by CS@Fc combined with NIR laser irradiation (Fig. 3F and S7). Fluorescently-labeled phalloidin binds and stabilizes filamentous actin, which was used to visualize cytoskeletal distribution in cells. Fig. S8 shows that KYSE70 cells exhibited robust morphology and extended pseudopodia without irradiation. Upon exposure to the NIR laser, the cytoskeletons of cells treated with CS or CS@Fc collapsed and shrunk.

The invasion and migration of tumor cells are pivotal factors influencing tumor metastasis and recurrence. Exposure to the NIR laser inhibited colony formation in KYSE70 cells, leading to decreased survival of colonies (Fig. 3G). In addition, transwell invasion and wound healing assays exposed that KYSE70 cells treated with CS@Fc in the presence of an NIR laser exhibited lower migration rates and significantly reduced invasive capabilities (Fig. 3H-I and Fig. S9).

Collectively, the collective results strongly support the assertion that CS@Fc exerted significant photothermal properties and cytotoxic effects on KYSE70 cells upon

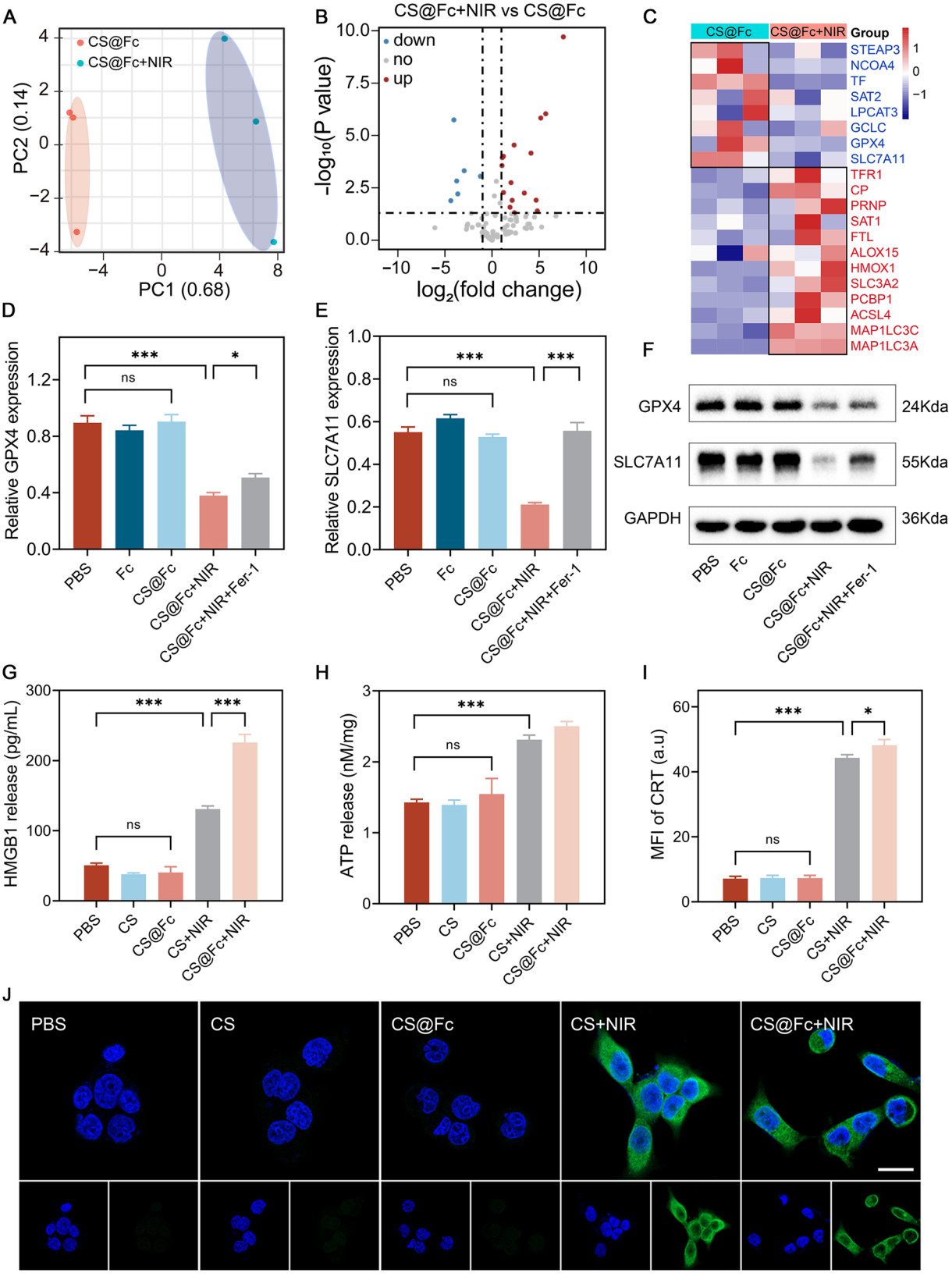

Fig. 2 (See legend on next page.)

(See figure on previous page.)

Fig. 2 (**A**) The UV-vis spectra of CS and CS@Fc NPs. (**B**) Photothermal curves of CS@Fc after NIR laser irradiation under different power densities. (**C**) Photothermal curves of CS@Fc with varying concentrations after NIR laser irradiation. (**D**) Thermal photographs of CS, CS@Fc and H_2O after NIR laser irradiation. (**E**) Heating-cooling curves of CS@Fc irradiated with NIR laser. (**F**) The photothermal effect of CS@Fc and the corresponding linear fitting curve. (**G**) Photothermal stability curve of CS@Fc. (**H**) UV-vis spectra of Fc surplus at different times. (**I**) Release profiles of Fc from the CS@Fc after irradiation for different periods

NIR laser exposure, highlighting its potential in antitumor therapies.

Ferroptosis-inducing capability of CS@Fc

The mechanism of action triggered by CS@Fc was also investigated. Ferro Orange, a novel fluorescent probe, was used to visualize Fe^{2+} within live cells [34]. As depicted in Fig. 4A and Fig. S10, minimal orange fluorescence was observed in the CS@Fc group, and the fluorescence intensity significantly increased after NIR laser irradiation, indicating the release of Fc carried Fe^{2+} from CS@Fc in response to elevated local temperatures. The TEM image in Fig. 4B displays the morphological changes in the mitochondria treated with CS@Fc. The morphology of mitochondria in the cells incubated with CS@Fc was expected, and characteristic features of ferroptosis, such as reduction in volume, thickening of the double membrane, and disappearance of mitochondrial cristae, were seen following NIR laser irradiation [35]. To assess the capacity of CS@Fc to induce ROS production in KYSE70 cells with high H_2O_2 expression, the fluorescent probe DCFH-DA was employed to evaluate various oxidative stressors. As displayed in Fig. 4C and Fig. S11A, cells treated with Fc, CS, and CS@Fc showed slightly increased green fluorescence compared to that of PBS, with no significant differences observed among the groups, demonstrating low intracellular ROS levels. However, the fluorescence intensity prominently enhanced under NIR laser irradiation, suggesting a notable rise in ·OH resulting from the Fenton/Fenton-like reaction, which further broke the redox balance. ROS production could contribute to lipid peroxidation by modulating the activity of the mitochondrial electron transport chain [36]. Additionally, we utilized the JC-1 probe to detect alterations in mitochondrial membrane potential ($\Delta\psi$) of KYSE70 cells after different treatments (Fig. 4D). Cells in the PBS group exhibited intense red fluorescence, signifying the aggregation of JC-1 within mitochondria in a manner reliant on normal potential. After NIR laser irradiation, the cells treated with CS demonstrated a modest elevation in green fluorescence, indicative of JC-1 translocation from the mitochondria to the cytoplasm. Conversely, the cells in the CS@Fc + NIR group displayed pronounced green fluorescence, expressing extensive mitochondrial impairment.

A key feature of ferroptosis is the accumulation of LPO products, resulting from ROS interactions with intracellular unsaturated fatty acids and ultimately leading to cell death. Utilizing the C11 BODIPY 581/591 probe, we observed a high level of green oxidized LPO fluorescence following CS@Fc combined irradiation. In contrast, cells in other non-irradiated groups exhibited red unoxidized LP fluorescence. Additionally, the green fluorescence of LPO was significantly reduced upon treatment with Ferrostatin-1 (Fer-1), which was considered as a ferroptosis inhibitor (Fig. 4E and Fig. S11B).

Malondialdehyde (MDA), a toxic byproduct of LPO, serves as a marker for lipid oxidation. As displayed in Fig. 4F, the MDA content in KYSE70 cells treated with CS@Fc in the presence of NIR laser showed approximately threefold compared to the CS@Fc-only group. In addition, the fluorescence value of cells supplemented with Fer-1 could be reinstated to their original levels in the absence of laser exposure, thereby reversing the alterations mentioned above. Thus, CS@Fc combined with the NIR laser irradiation induced ferroptosis in tumor cells by promoting ROS and LPO accumulation.

Mechanisms of ferroptosis induced by CS@Fc

Ferroptosis PCR arrays were employed to screen for the expression of critical effectors at the transcriptional level. Principal component analysis (PCA) based on 93 quantified factors distinctly separated cells treated with CS@Fc from those treated with CS@Fc + NIR, implying significant differences in gene expression between the two groups (Fig. 5A). As displayed in Fig. 5B, compared to CS@Fc, cells subjected to NIR laser irradiation exhibited differential expression of 21 genes ($FC > 1$, $p < 0.05$), with 15 genes significantly upregulated and 6 genes downregulated. Moreover, heatmap analysis depicted the crucial gene expression signatures of ferroptosis (Fig. 5C), including GPX4, SLC7A11, and GCLC, demonstrating the inactivation of the antioxidant system. Notably, the upregulation of TFR1, FTL, and STEAP3 indicated enhanced intracellular iron accumulation, thereby increasing susceptibility to ferroptosis. Among these genes, GPX4 is particularly critical in the regulation of ferroptosis. It effectively mitigates ferroptosis by directly reducing excess intracellular LPO to harmless lipid alcohols, thereby maintaining cellular homeostasis. Following treatment with CS@Fc combined with NIR laser irradiation, the mRNA levels of GPX4 were suppressed (Fig. S12). Reduced GSH, serving as a cofactor for GPX4, is a crucial intracellular reducing molecule that is depleted under oxidative stress induced by Fenton/Fenton-like reactions. Additionally, GSH synthesis

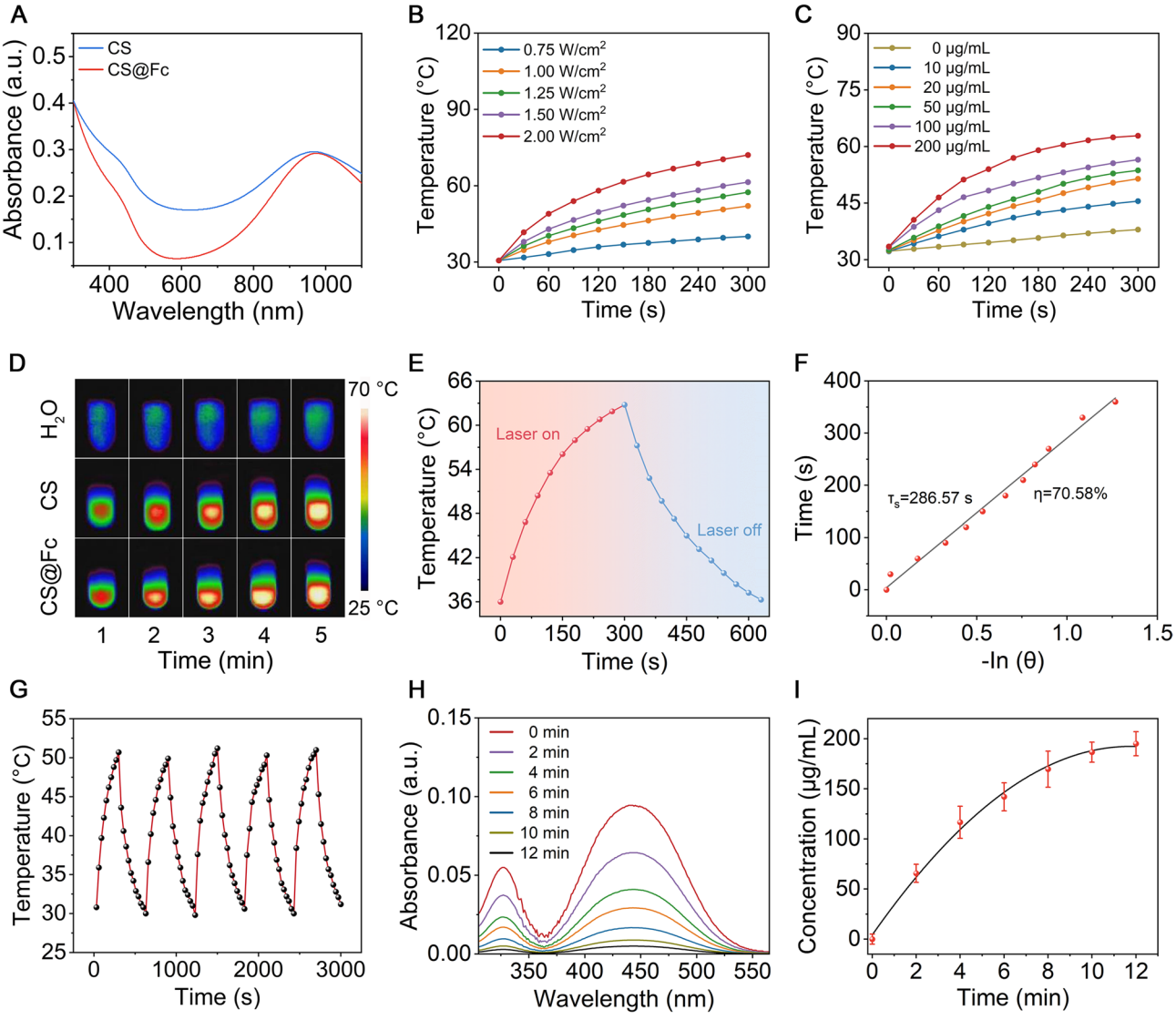

Fig. 3 (**A**) Cytotoxicity of different concentrations of CS@Fc in KYSE70 cells. (**B**) Relative viabilities of KYSE70 cells after various treatments. (**C**) LDH release assay of KYSE70 cells after various treatments. (**D**) Confocal microscopy images of CS@DiD in KYSE70 cells. Scale bar: 20 μm. (**E**) Calcein/PI fluorescent staining of KYSE70 cells with various treatments. Scale bars: 100 μm. (**F**) Cell apoptosis of KYSE70 cells with various treatments. (**G**) Colony formation, (**H**) invasion assay and (**I**) wound healing results of KYSE70 cells with various treatments

relies on the translocation of cysteine facilitated by the antiport mechanism of system Xc^-, involving heterodimers SLC7A11 (xCT) and SLC3A2 linked by disulfide bonds. Thus, monitoring these three indicators reflects the changes in intracellular antioxidant levels. Western blot analysis (Fig. 5D-F) revealed a significant down-regulation of GPX4 and SLC7A11 expression following treatment with CS@Fc in the presence of NIR laser, while pre-treatment with Fer-1 led to increased protein expression in KYSE70 cells. Further analysis found alterations in the intracellular GSH levels, indicating increased GSH consumption after treatment with CS@Fc and NIR laser irradiation, leading to GPX4 inactivation and disruption of the antioxidant system.

Immune activation effect of CS@Fc

Previous reports have demonstrated that PTT can induce ICD in tumor cells [37]. Additionally, tumor cells express pronounced immunogenicity as they undergo ferroptosis, emitting a cascade of immunostimulatory cues referred to as "find me" and "eat me" signals, notably including the release of damage-associated molecular patterns (DAMPs) [38]. To investigate the possible influence of CS@Fc on the immunogenicity of tumor cells, we examined the release of DAMPs after various interventions. An enzyme-linked immunosorbent assay (ELISA) was used to determine the release of high mobility group box 1 (HMGB1). The levels of HMGB1 were elevated to 133.9 pg/mL in the CS group and 225.7 pg/mL in the

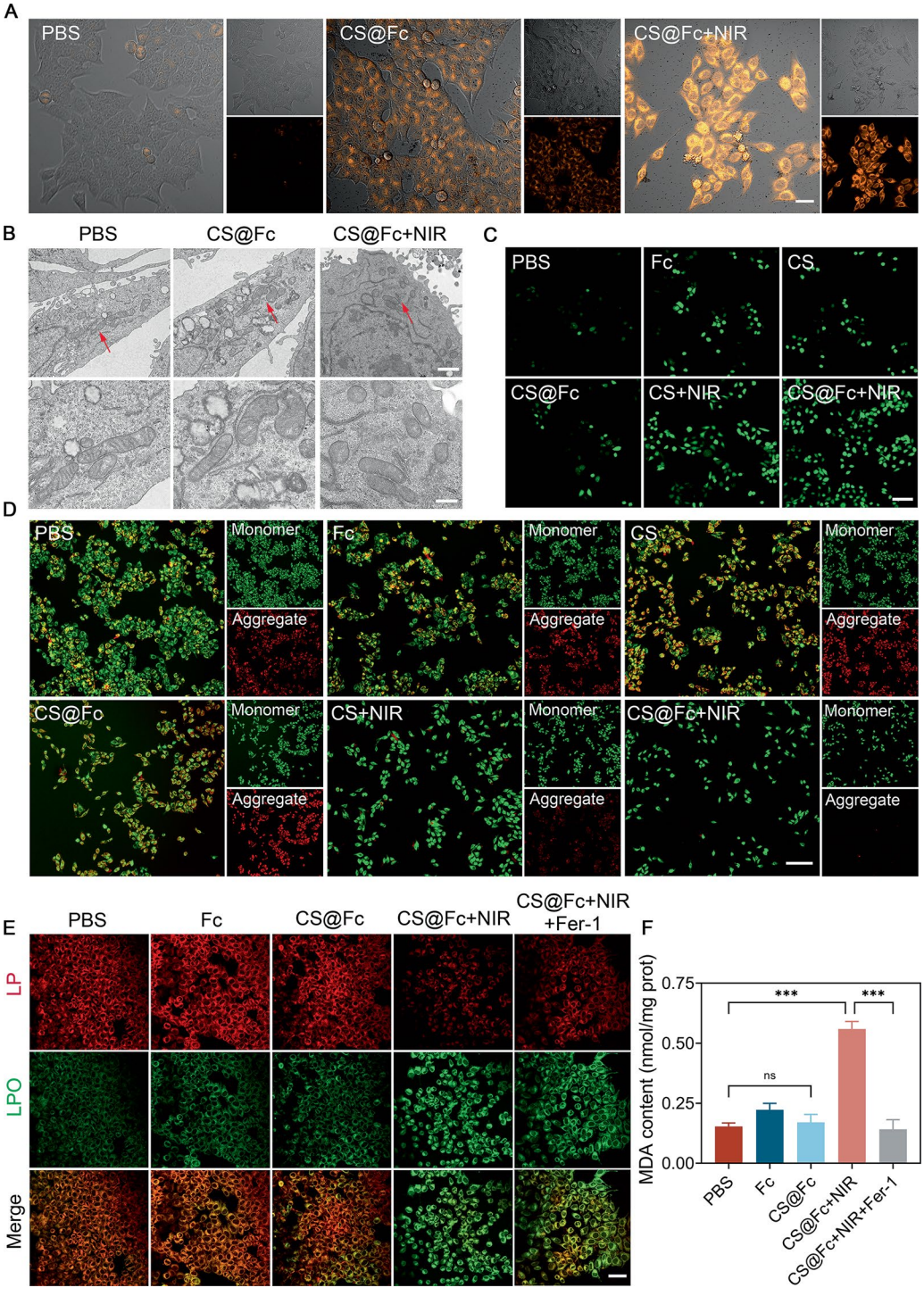

Fig. 4 (**A**) Confocal fluorescence images of cellular Fe^{2+} content in KYSE70 cells. Scale bar: 50 μm. (**B**) TEM images of mitochondrial morphological changes in KYSE70 cells. Scale bar: 400 nm. (**C**) Fluorescence images of ROS generation and effect on mitochondrial membrane potential in KYSE70 cells detected by DCFH-DA and (**D**) JC-1 staining with various treatments. Scale bar: 100 μm. (**E**) Fluorescence images of LPO in KYSE70 cells with various treatments. Scale bar: 50 μm. (**F**) MDA content of KYSE70 cells after various treatments

CS@Fc group when subjected to NIR laser irradiation. This finding suggested that the combined application of PTT with ferroptosis markedly enhanced the release of HMGB1 (Fig. 5G). Changes in adenosine triphosphate (ATP) secretion exhibited a trend similar to that of HMGB1, as observed through chemical fluorescence (Fig. 5H). Green fluorescence originating from calreticulin (CRT) was observed along the membrane of cells

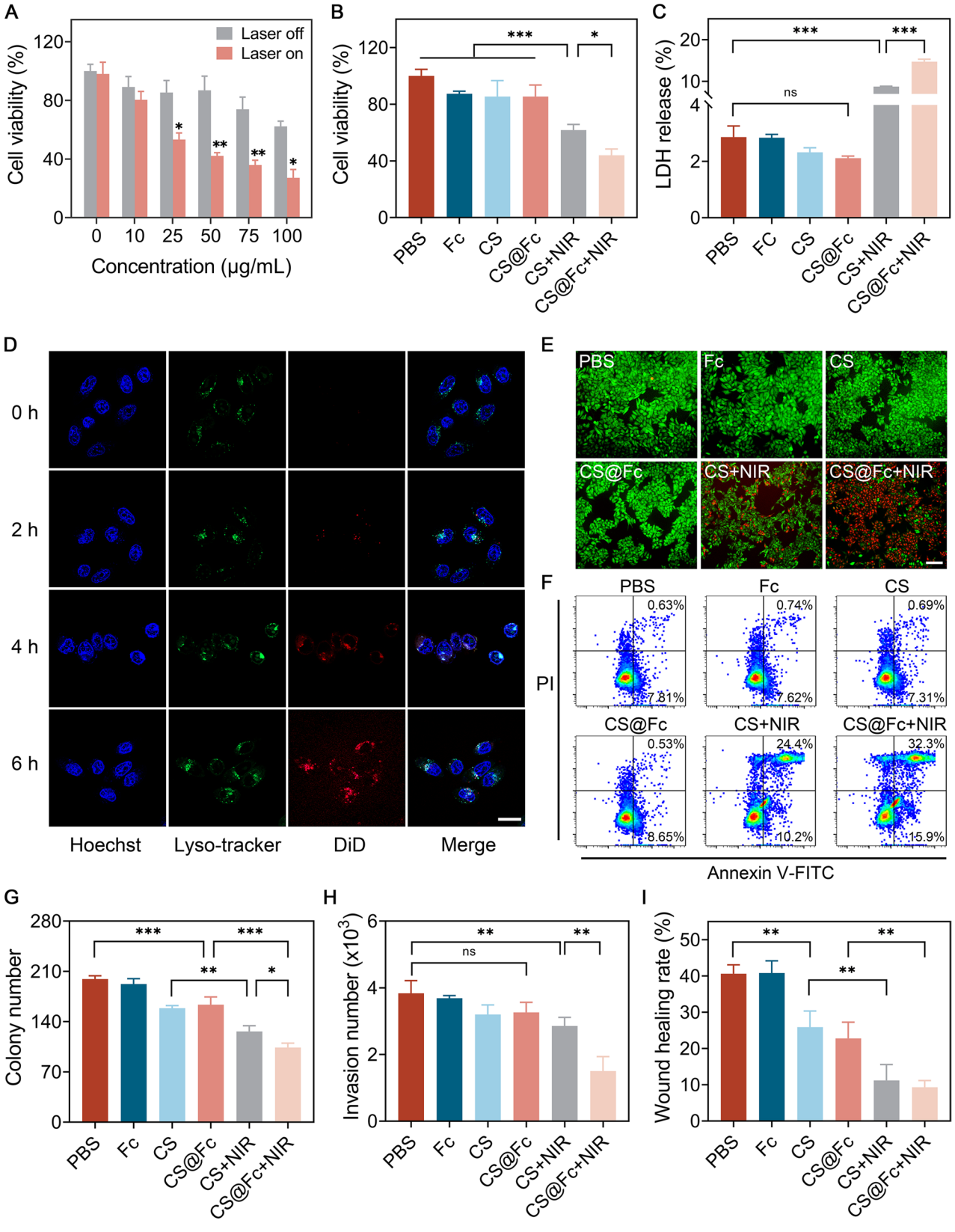

Fig. 5 (See legend on next page.)

(See figure on previous page.)

Fig. 5 (**A**) PCA of the differentially expressed genes in the CS@Fc and CS@Fc + NIR groups. (**B**) Volcano plot of the differentially expressed genes in the CS@Fc and CS@Fc + NIR groups (FC ≥ 1.0, $p < 0.05$). (**C**) Heat map of genes in the CS@Fc and CS@Fc + NIR groups. Quantitative analysis of the expression of (**D**) GPX4 and (**E**) SLC7A11 expression with various treatments in KYSE70 cells and (**F**) western blot assay. (**G**) HMGB1 release and (**H**) ATP secretion from KYSE70 cells after various treatments. (**I**) Confocal fluorescence quantification and (**J**) images of CRT in KYSE70 cells after various treatments. Scale bar: 150 μm

subjected to either CS or CS@Fc combined irradiation (Fig. 5I-J). Concurrently, free CS or CS@Fc did not affect CRT exposure, confirming the effective induction of ICD by CS@Fc combined irradiation.

In vivo photothermal effect and distribution of CS@Fc

The photothermal efficacy of CS@Fc was validated to assess its therapeutic potential in vivo. Initially, tumor-bearing mice were intratumorally injected with saline, CS, and CS@Fc, followed by NIR laser irradiation. As depicted in Fig. 6A, the surface temperature of tumors intratumorally injected with CS@Fc rapidly increased from 35 °C to 45 °C within 150 s observed by IR thermal imaging camera, whereas mice injected with saline exhibited only a 2 °C temperature rise (Fig. 6B), confirming the noteworthy photothermal effects of CS@Fc in vivo.

Before the treatment of mice, a hemolysis assay was conducted to verify the suitability of the prepared NPs for intravenous administration. As displayed in Fig. 6C, no hemolytic reaction was observed when incubated with different concentrations of CS@Fc, confirming the excellent blood compatibility of CS@Fc for intravenous injection. Subsequent experiments involved labeling CS NPs with a fluorescence dye DiR for real-time tracking and visualization, evaluating the tumor-targeting ability and biodistribution behavior of CS@DiR in vivo. After intravenous injection at different time points, KYSE70 tumor-bearing mice were imaged using in vivo imaging systems at specific excitation wavelengths. Mice injected with free DiR did not display significant fluorescence at any time point, likely due to the rapid clearance of the small molecule DiR. CS@DiR exhibited fluorescence signals at the tumor site from 8 h post-injection, gradually intensifying over time (Fig. 6D-E). At 48 h post-injection, the tumor and major organs of mice from each group were dissected for ex vivo fluorescence imaging (Fig. 6F). Semi-quantitative results (Fig. 6G) showed that fluorescence mainly accumulated in the tumor. The average fluorescence intensity at the tumor site in the CS@DiR group was 18.7 times compared to that in the free DiR group, indicating efficient accumulation of CS@DiR at tumor sites via the enhanced permeability and retention (EPR) effect with reduced clearance [39, 40]. Similar conclusions were validated in AKR tumor-bearing mice (Fig. S13-15).

In vivo antitumor activity of CS@Fc

In vitro investigations confirmed the robust antitumor efficacy and immunostimulatory properties of CS@Fc. Consequently, we evaluated the therapeutic impact of CS@Fc on the subcutaneous tumor model using KYSE70 cells. Tumor volume was monitored and recorded over time. KYSE70 tumor-bearing mice were administered intratumorally of CS@Fc followed by NIR laser irradiation 30 min later (Fig. 7A). Throughout the treatment period, the body weight of the mice remained relatively stable, indicating the high safety profile of CS@Fc NPs (Fig. 7B). At the experimental endpoint, mice were euthanized, the tumor tissues were carefully excised, photographed, and weighed (Fig. 7C). After five treatments, the tumor suppression rate for each group was calculated. The non-irradiated group demonstrated significantly poorer tumor suppression capabilities compared to the CS@Fc + NIR group, which achieved a suppression rate of 46.13%. Additionally, mice pretreated with GSH showed a decreased tumor suppression rate compared to the CS@Fc + NIR group. As shown in Fig. 7D-E, the trends in the average tumor weight and volume were consistent with the observed suppression rates. The CS@Fc + NIR group displayed the most pronounced antitumor effect, evidenced by the smallest tumor volumes and weights recorded. After the final treatment for 6 h, GSH content was assessed using a GSH detection kit, and the results revealed a significant decrease in the CS@Fc + NIR group (Fig. S16), while minor changes in GSH consumption were observed when mice were treated with CS@Fc alone. To further prove the tumor ablation efficacy of CS@Fc, tumor sections from each group were subjected to histopathological examination. The hematoxylin and eosin (H&E) staining results are displayed in Fig. 7F. Compared to the other groups, tumor tissue in the CS@Fc + NIR treatment group exhibited typical histopathological damage, including nuclear condensation and fragmentation. In addition, Ki-67 staining indicated minimal proliferation in this group. Fluorescence detection of caspase-3 and TdT-mediated dUTP nick-end labeling (TUNEL) indicated a significant apoptosis signal in the CS@Fc + NIR group. Remarkably, the expression of GPX4 was significantly upregulated in the CS@Fc + NIR treatment group, suggesting that the combination of CS@Fc combined with NIR laser irradiation could disrupt the antioxidant system within the TME, leading to oxidative damage to the tumor, further indicating the induction of ferroptosis in vivo.

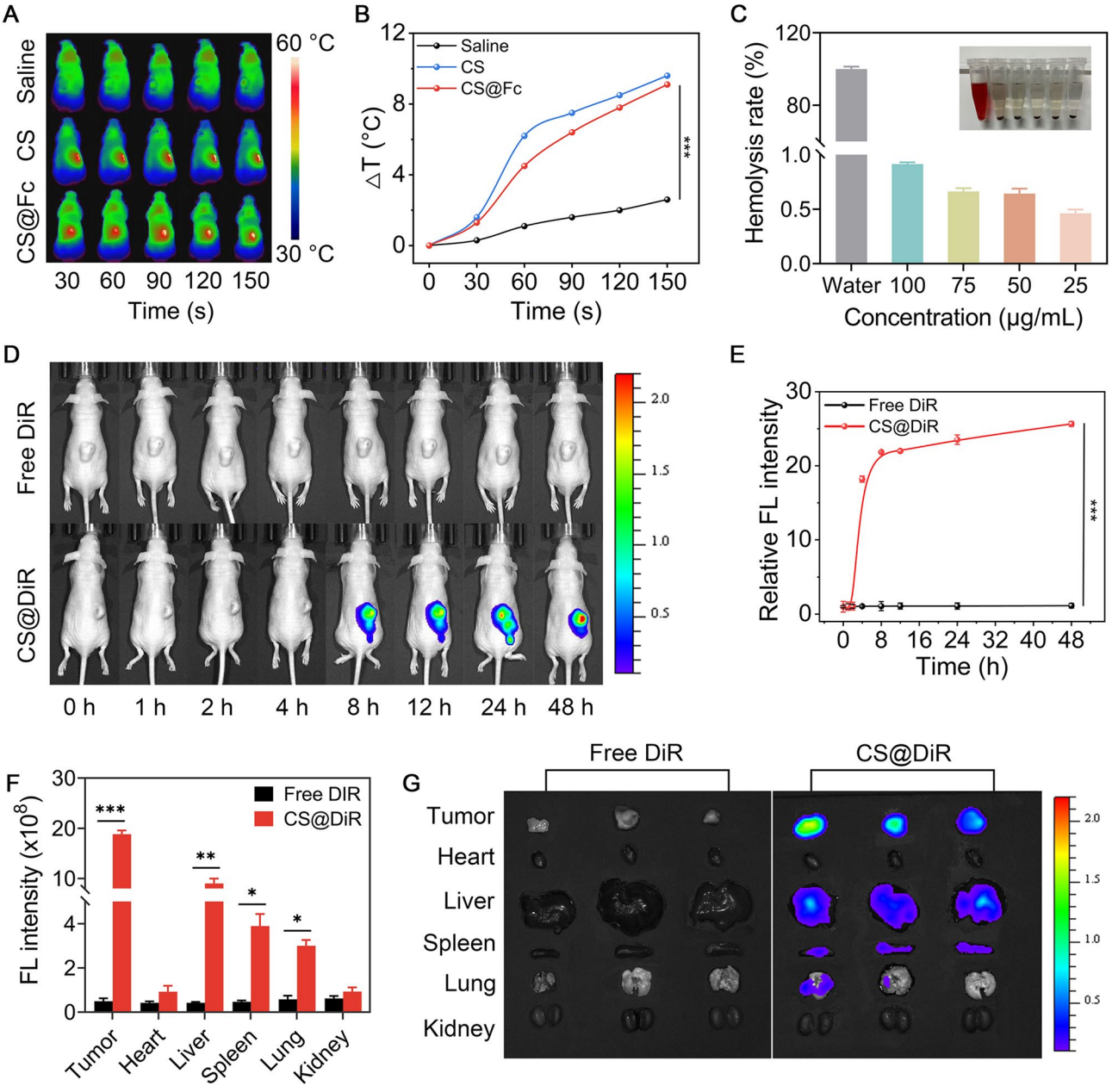

Fig. 6 (**A**) IR thermal images by exposing tumors of mice to irradiation (980 nm, 0.5 W/cm^2) after injection of Saline, CS and CS@Fc. (**B**) Temperature elevation curves at different times. (**C**) Hemolysis tests of different concentrations of CS@Fc NPs. (**D**) In vivo fluorescent images of mice at specific time points after *i.v.* injected with CS@DiR and free DiR. (**E**) The radiant intensity of tumor measured at time intervals. (**F**) Semi-quantification of fluorescent intensity and (**G**) ex vivo fluorescent images of tumors and major organs

Furthermore, we established subcutaneous tumor model in C57BL/6 mice to investigate the effect of CS@Fc on AKR tumor ablation (Fig. 8A). While the CS@Fc + NIR group exhibited the highest antitumor capabilities with a suppression rate of approximately 62.22% (Fig. 8B-D), reconfirming the therapeutic efficacy of CS@Fc combined with NIR laser irradiation. The body weight of the mice gradually increased during the treatment period, indicating no significant adverse effects of CS@Fc in vivo (Fig. 8E).

In vivo antitumor immune responses

PTT has been shown to trigger ICD in tumor cells, resulting in the release of tumor-associated antigens (TAAs) and DAMPs, which in turn provoke robust antitumor immune responses [9, 41-43]. In addition, the release of TAAs from cancer cells undergoing ferroptosis can further enhance the antitumor immune response [44, 45]. Consequently, nanotechnology-mediated modulation of ferroptosis is expected to counteract

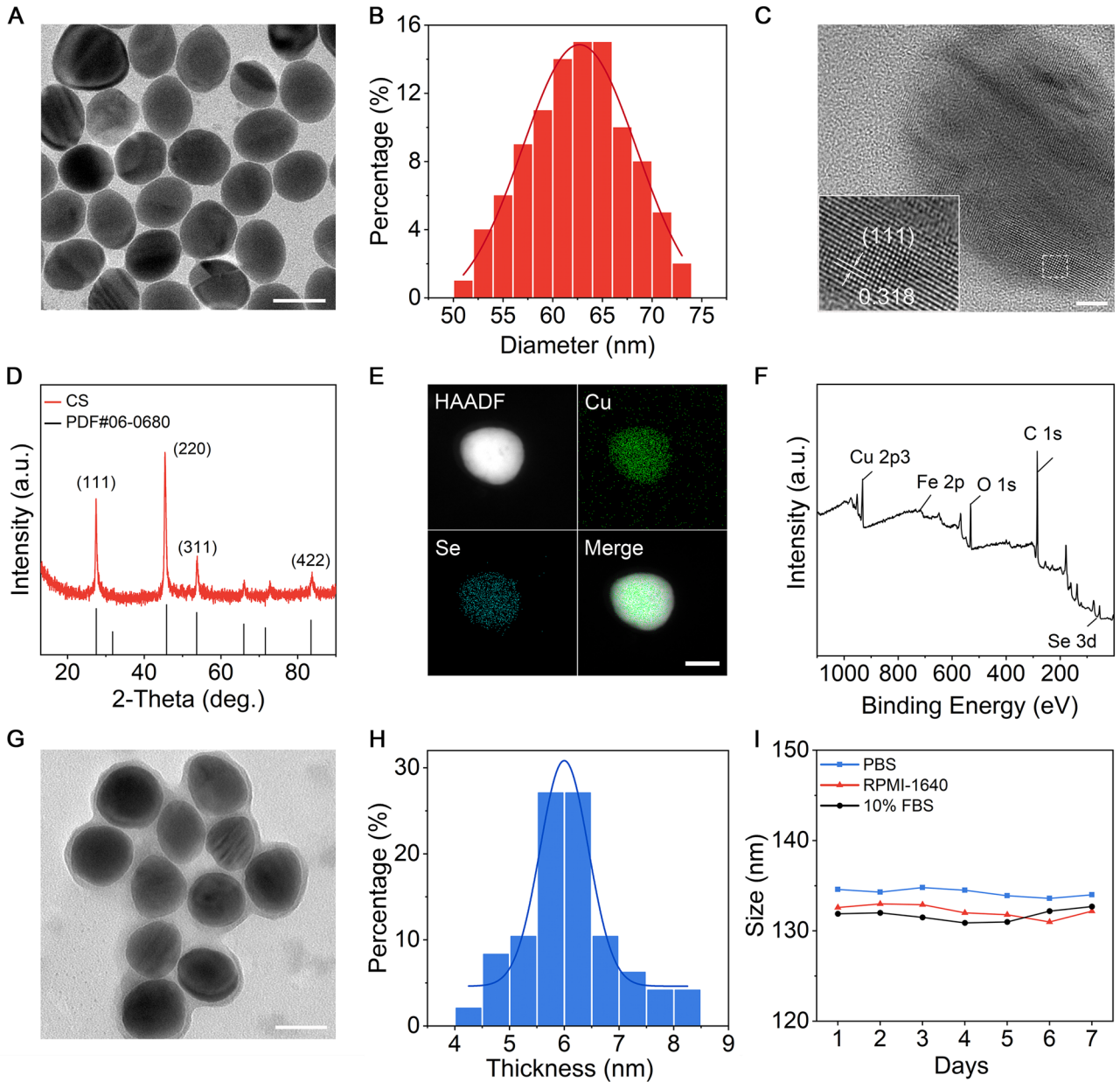

Fig. 7 (**A**) Schematic illustration of the treatment protocol in KYSE70 tumor-bearing mice. (**B**) Tumor excised weight in each group after different treatments ($n = 6$). (**C**) Photographs of tumors excised from KYSE70 tumor-bearing mice. (**D**) Average tumor growth curves of tumors in each group after different treatments. (**E**) Average body weight of mice with various treatments. (**F**) Histological images of tumor slices stained with H&E, TUNEL, antigen Ki-67, GPX4, and caspase-3 after different treatments. Scale bar: 50 μm

the immunosuppressive tumor microenvironment and enhance the efficacy of tumor immunotherapy.

To investigate whether CS@Fc-based PTT and ferroptosis could enhance immune surveillance and thereby contribute to the antitumor efficacy, single-cell suspensions from tumor-draining lymph nodes subjected to various treatments were collected and analyzed using flow cytometry to assess alterations in the tumor immune microenvironment. The maturation of DCs is essential for initiating, regulating, and maintaining adaptive immune responses [46]. Figure 8F displays the DC maturation level in the TME under different treatments. The CS@Fc alone displayed no significant effect on DC maturation. The percentage of mature DC ($CD11c^+$ $MHC\text{-}II^+$) increased to 5.81% in the CS@Fc + NIR group and 5.02% in the CS + NIR group, probably due to the combined effect of PTT and ferroptosis. The activation of DC can stimulate CTLs, thereby enhancing adaptive immune responses against tumors. Flow cytometry analysis (Fig. 8G-H) showed that CS@Fc + NIR treatment

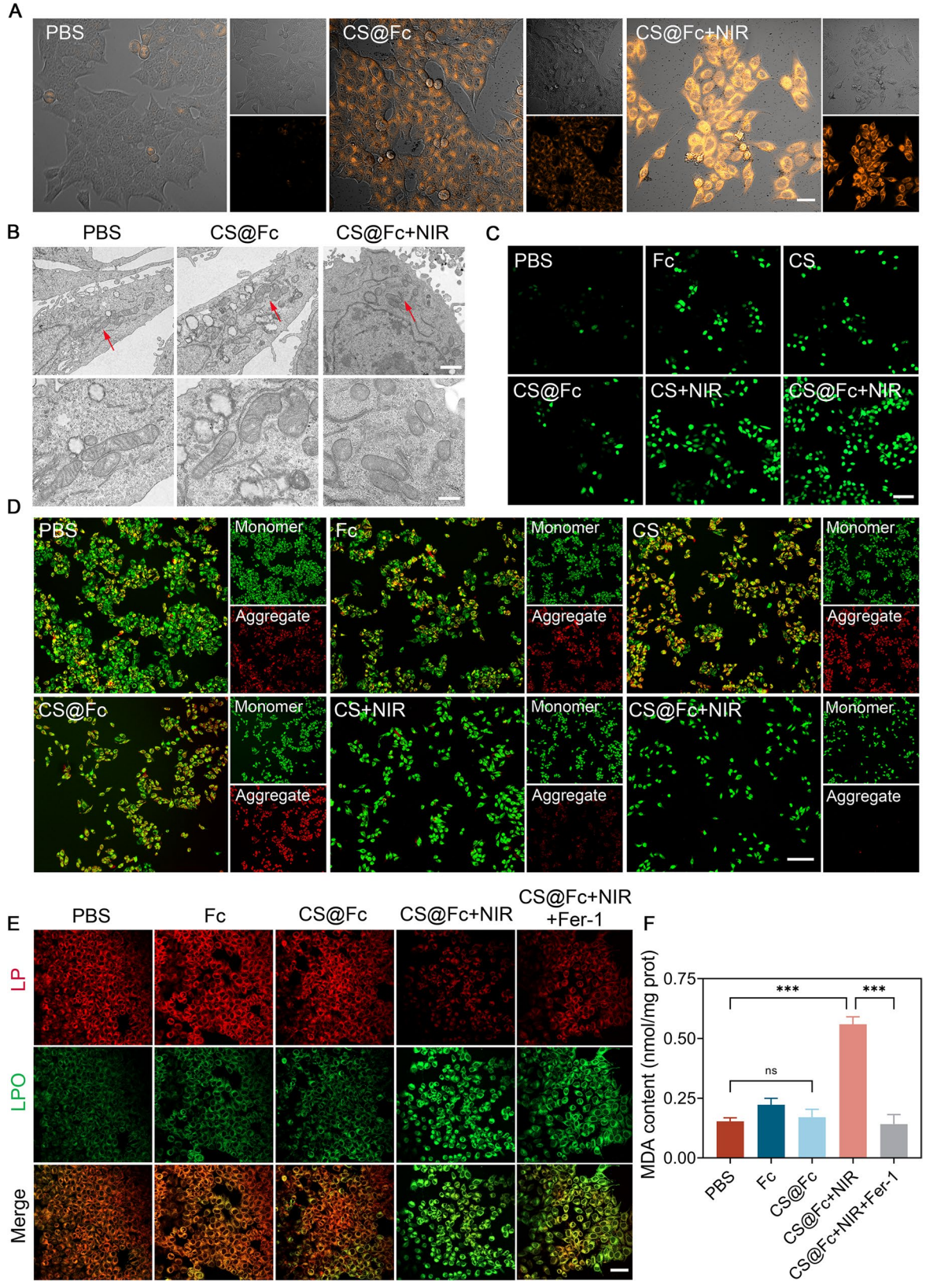

Fig. 8 (**A**) Schematic illustration of the treatment protocol in AKR tumor-bearing mice. (**B**) Tumor excised weight in each group after various treatments. (**C**) Photographs of tumors excised from AKR tumor-bearing mice. (**D**) Average tumor growth curves of tumors in each group after various treatments. (**E**) Average body weight of mice after various treatments. (**F**) Flow cytometric statistical analysis of the percentages of DC maturation, (**G**) $CD3^+$ $CD4^+$ T cells, (**H**) $CD3^+$ $CD8^+$ T cells and (**I**) $INF\text{-}\gamma^+$ $CD8^+$ T cells

downregulated the expression frequencies of $CD3^+$ $CD4^+$ T cells while concurrently upregulated $CD3^+$ $CD8^+$ T cells in the TME. Notably, $CD8^+$ T cells were activated to CTLs upon stimulation, exhibiting a similar upregulation trend (Fig. 8I). The proportion of CTLs in the CS@Fc + NIR group was over threefold greater than that of the Saline group, exhibiting a more substantial synergistic effect compared to photothermal stimulation alone. To further explore the potential of CS@Fc-based PTT and ferroptosis in enhancing immune surveillance and contributing to antitumor efficacy, we also examined the proportion of regulatory T cells (Tregs) within tumor-draining lymph nodes. Flow cytometry analysis indicated a marked decrease in the ratio of $CD4^+CD25^+Foxp3^+$ Tregs following CS@Fc + NIR treatment compared to CS + NIR or CS@Fc treatment alone (Fig. S17). These findings suggest that the combination of CS@Fc and NIR laser irradiation effectively stimulates antitumor immune responses and mitigates the immunosuppressive tumor microenvironment, ultimately leading to a favorable antitumor effect.

In addition, the integration of PTT with immunotherapy not only significantly enhances immunogenicity but also effectively reduces immunosuppression, thereby exhibiting superior synergistic therapeutic efficacy. To elucidate the antitumor mechanism of CS@Fc-based PTT in combination with Anti-PD-1 blockade, we established a subcutaneous AKR tumor-bearing mouse model to investigate the synergistic therapeutic efficacy in terms of tumor ablation and remodeling of the tumor immune microenvironment. The schedule for the in vivo experimental design is presented in Fig. S18A. A single administration of Anti-PD-1 blockade demonstrated limited therapeutic efficacy compared to the saline-treated control group (Fig. S18B). In comparison, the combined treatment of CS@Fc + NIR and Anti-PD-1 blockade led to a significant reduction in both tumor size and the weight of excised tumors, as illustrated in Fig. S18C-D. Furthermore, the overall increase in body weight of the mice suggests that the treatment exhibits favorable biosafety (Fig. S18E). For immune stimulatory efficacy analysis, tumor-infiltrating lymphocytes from mice subjected to various treatments, including Anti-PD-1 blockade alone or in combination with CS@Fc + NIR, were examined using flow cytometry (Fig. S18F-H). The results indicated that Anti-PD-1 blockade increased the proportion of CTLs while decreasing the proportion of Tregs within the tumor immune microenvironment. The administration of CS@Fc + NIR further enhanced the effects of Anti-PD-1 blockade by effectively stimulating the proliferation and activation of CTLs and mature DCs, which was evidenced by the recruitment of a higher proportion of $IFN\text{-}\gamma^+CD8^+$ cells in $CD3^+$ T cells and $CD80^+MHC\text{-}II^+$ cells in $CD11c^+$ cells in the tumor-draining lymph nodes (Fig. S18F-H). This combination demonstrated a favorable synergistic effect, eliciting a robust antitumor immune response, thereby inhibiting tumor growth and enhancing the antitumor efficacy of Anti-PD-1 blockade.

At the end of treatment, the mice were euthanized, and tumor tissues from each experimental group were collected for histopathological, immunohistochemical and immunofluorescence analysis. H&E staining demonstrated significant apoptosis and necrosis in tumor cells from the CS@Fc + NIR treatment group, with reduced Ki-67 positivity rate and elevated percentage of TUNEL positivity, indicating elevated levels of apoptosis (Fig. S19). Besides, previous studies have demonstrated that moderate hyperthermia induced by PTT can enhance the intratumoral blood flow, thereby improving overall tumor oxygenation and alleviating hypoxic conditions within the tumor [47–49]. The immunofluorescent staining of HIF-1α, a transcription factor that responds to oxygen availability and serves as a well-established biomarker of hypoxia, as depicted in Fig. S20, illustrates that hypoxic signals within the tumor microenvironment were markedly reduced following NIR laser irradiation. These findings suggest that CS@Fc-based PTT is capable of effectively mitigating hypoxic conditions within the tumor, thereby enhancing therapeutic efficacy. Overall, these findings substantiate the superior therapeutic efficacy of the CS@Fc system in combination with NIR laser irradiation in vivo.

In vivo biosafety of CS@Fc

To investigate the biocompatibility of CS@Fc, the major organs (heart, liver, spleen, lung, and kidney) of the treated mice were collected at the experimental endpoint. Histological examination using H&E staining was conducted to assess the impact of CS@Fc administration on these major organs, thereby evaluating its in vivo toxicity. The results displayed in Fig. S21 and Fig. S23 showed that the cellular morphology of the major organ tissues in each treatment group remained intact without significant changes. Concurrently, blood samples were collected from the mice in each group to analyze. Blood routine parameters were within normal ranges, indicating no significant induction of infection or inflammation during the treatment. Further assessment of hepatic and renal functions using biochemical markers showed no adverse effects (Fig. S22 and Fig. S24). Accordingly, CS@Fc NPs in photothermal ferroptosis combination therapy demonstrated favorable in vivo safety profiles.

Conclusions

This study aims to investigate the photothermal conversion capabilities of CS NPs. We successfully encapsulated the ferroptosis inducer Fc using a thermo-responsive ligand LA onto CS NPs, thereby developing a novel CS@

Fc nano-delivery system for the combined photothermal-ferroptosis therapy of EC. Under acidic TME conditions and NIR laser stimulation, CS@Fc released Fc and Cu^{2+}, triggering Fenton/Fenton-like reactions and generating a substantial amount of ·OH, which disrupted cellular redox homeostasis. Simultaneously, significant depletion of GSH inhibited the system Xc^-/GPX4 signaling pathway, further promoting LPO accumulation and ultimately leading to cell death. Additionally, CS@Fc-based PTT was found to induce ICD by releasing a series of cytokines, enhancing the recruitment of CTLs, stimulating DC maturation, and suppressing Treg infiltration. Consequently, it exhibited a favorable synergistic effect with Anti-PD-1 blockade, effectively eliciting a robust antitumor immune response and facilitating tumor eradication. Additionally, CS@Fc effectively accumulated in tumor sites and exhibited significant therapeutic efficacy through a synergistic mechanism. Furthermore, multiple safety assessment experiments confirmed the excellent biocompatibility of CS@Fc, highlighting its potential for clinical translation and application.

Materials and methods

Chemicals and reagents

Selenous acid (H_2SeO_3, >99.99%), polyvinyl pyrrolidone (PVP, MW≈55,000), copper chloride ($CuCl_2$, >98%), L-ascorbic acid (AA, >99.7%), lauric acid ($C_{12}H_{24}O_2$, ≥98%) were obtained from Sigma-Aldrich (St. Lous, MO). *N*, *N*-Dimethylformamide (DMF, ≥99.5%), hydrazine hydrate ($N_2H_4{\cdot}H_2O$, 80%), and ferrocene ($FeC_{10}H_{10}$, 99%) were purchased from Shanghai Macklin Biochemical Co., Ltd.

Preparation of CS@Fc NPs

Synthesis of Se nanospheres: 0.374 g of H_2SeO_3 and 0.2 g of PVP were dissolved sequentially in 100 mL of deionized (DI) water. Then, 1 mL of $N_2H_4{\cdot}H_2O$ was added to the mixture. After 5 h, the resulting solid product was centrifuged at 12,000 rpm for 10 min. Solid products were washed and dispersed with DI water.

Synthesis of CS NPs: The synthesis process commenced by sequentially introducing Se nanospheres dispersion (1 mg/mL), PVP solution (10 mg/mL), $CuCl_2$ solution (0.1 M), and AA solution (0.1 M) into the beaker. After 5 min, 40 μL of H_2O_2 was added to the mixture. The resultant product underwent centrifugation at 12,000 rpm for 10 min. The solid products were washed and dispersed in DI water.

Synthesis of CS@Fc NPs: 0.2 g of Fc and 0.25 g of LA were sequentially dissolved in 1 mL of DMF. Subsequently, 3 mg of CS was dispersed into the solution and stirred for 2 h. The resulting product was centrifuged to remove the supernatant and dispersed with DI water.

Characterization of CS@Fc NPs

The morphologies of CS and CS@Fc NPs were characterized by TEM (JEOL, JEM-2100, Japan). The chemical phase compositions were analyzed using XRD (Bruker, D8 ADVANCE, Germany). XPS (Thermo Fisher ESCALAB 250XI, USA) was conducted to identify the chemical states of elements of CS@Fc. The absorption spectra of the CS and CS@Fc NPs were recorded using a UV-vis spectrophotometer (Shimadzu, UV-2600, Japan). The hydrodynamic diameter was measured by zetasizer (Malvern, Nano ZS90, UK).

The photothermal effect of CS@Fc NPs

To investigate the photothermal performance, CS, CS@Fc aqueous suspension, and DI water were irradiated by a continuous 980 nm laser for 5 min. Thermal photographs were taken using an IR thermal camera (HIKMICRO, H11 pro, China). Moreover, the photothermal stability of CS@Fc was evaluated through five cycles (980 nm, 1.0 W/cm^2). The photothermal conversion efficiency (η) was calculated according to the formula:

$$\eta = \frac{m \times c \times (T_{max} - T_{surr})}{I \times (1 - 10^{-A}) \times \tau_s}$$

m, c, T_{max}, T_{surr}, A, τ_s stand for the solution mass, the heat capacity of water (4.2 J/g), the maximum temperatures reached by the CS@Fc, the room temperature, the absorbance of the CS@Fc NPs at 980 nm, the system time constant determined through linear regression of the cooling profile respectively.

Determination of Fc release

After 0, 2, 4, 6, 8, 10, and 12 min of 980 nm laser exposure, the CS@Fc dispersion was centrifuged to remove the supernatant. The resulting solid was then dispersed in DMF to fully release Fc, followed by another centrifugation to collect the supernatant for UV-vis absorption testing. By fitting the UV-vis absorption values into the standard curve of Fc, the residual amount of Fc encapsulated after each irradiation time was determined.

Cell culture

KYSE70 cells were cultured in RPIM-1640 medium containing with 10% FBS and 10,000 U/mL of penicillin-streptomycin. HUVEC and AKR were cultured by DMEM with 10% FBS and 10,000 U/mL of penicillin/streptomycin. All cells were cultured at 37 °C in a 5% CO_2 incubator.

Cell viability assay

The cell viability was determined using a CCK-8 (Invigentech). KYSE70 or HUVEC cells (5.0×10^3) were seeded on 96-well plates and incubated with different

concentrations of CS@Fc. After 24 h, half of the cells in each group were irradiated by the 980 nm laser to maintain a temperature of 45 °C for 5 min. Finally, the absorbance at 450 nm was recorded using a microplate reader (BioTek, Epson, USA).

LDH release assay

KYSE70 cells (5.0×10^3) were seeded on 96-well plates and pretreated with different formulations. After 24 h, half of the cells in each group were irradiated by the 980 nm laser to maintain a temperature of 45 °C for 5 min. The amount of LDH released was evaluated by a commercial kit (Dojindo). The absorbance at 490 nm was recorded using a microplate reader.

Cellular uptake assay

CS@Fc was fluorescently labeled by DiD. KYSE70 cells (5.0×10^3) were incubated with CS@DiD (50 μg/mL). At 0, 2, 4, and 6 h, cells were fixed with 4% paraformaldehyde (PFA), stained with Lyso-tracker (AAT Bioquest) and Hoechst 33,342 (Beyotime) respectively, and the intracellular fluorescence was measured by CLSM (Zeiss, LSM-800, Germany).

Apoptosis assay

KYSE70 cells (2.0×10^5) were seeded on 12-well plates and pretreated with different formulations. After 24 h, half of the cells in each group were exposed to a 980 nm laser. Then, the cells were incubated with Annexin V-FITC/PI (KeyGen Biotech) reagent. Fluorescence intensities were examined by flow cytometer (Cytek, NL-CLC, USA) and analyzed.

Calcein AM/PI staining

KYSE70 cells (1.0×10^5) were seeded on 12-well plates and pretreated with different formulations. After 24 h, half of the cells in each group were exposed to a 980 nm laser. The cells were further incubated with a Calcein AM/PI reagent (Beyotime), and the cell survival/death was assessed by an inverted microscope (Thermo Fisher Scientific, Evos M7000, USA).

Cell morphology

KYSE70 cells (5.0×10^3) were seeded on 12-well plates and incubated with CS and CS@Fc for 24 h. Then half of the cells in each group were exposed to a 980 nm laser. Subsequently, the cells were then fixed with 4% PFA. Then the cells were incubated with phalloidin-TRITC (AAT Bioquest) in the humidifying box, and stained with DAPI. The fluorescence images were measured by CLSM.

Colony formation assay

KYSE70 cells (1.0×10^3) were seeded on 12-well plates. After 3 days, the cells of irradiation groups were exposed to a 980 nm laser. Then the cells were fixed with 4% PFA, and stained by 0.1% crystal violet (Beyotime). Images of the cell colonies of different treatments were captured using an inverted microscope (Nikon, Eclipse Ti, Japan).

Cell invasion assays

KYSE70 cells (1.5×10^5) cultured in a 12-well plate. After different treatments, the cell suspension was inoculated into the upper chamber (precoated with Matrigel) and 500 μL completed medium was added to the lower chamber. After 48 h, the migrated cells were fixed using 4% PFA and treated with 0.1% crystal violet for staining. The images were captured using an inverted microscope.

Wound healing assay

KYSE70 cells (1.5×10^5) were seeded in 12-well plates to allow for adherence. A scratch was created in the cell monolayer using a 200 μL sterile micropipette tip to simulate a wound. Then cells were treated with different formulations, following the exposure to 980 nm laser of the irradiation groups. Finally, the wound healing process was monitored and photographed by a microscope.

Intracellular ferrous ion (Fe^{2+}) level assay

The intracellular Fe^{2+} level was detected by utilizing a FerroOrange probe (Dojindo). KYSE70 cells (5.0×10^3) were seeded into the confocal dish for 48 h. Then, the cells were washed with PBS and incubated with CS@Fc (50 μg/mL) for another 24 h, then exposed to a 980 nm laser. Finally, the FerroOrange probe (1 μM) was added and incubated for 30 min, followed by washing with PBS and imaged by CLSM.

Mitochondria morphology analysis

KYSE70 cells (1.0×10^5) were seeded into 12-well plates and then subjected to different treatments. After 24 h, cells were collected, fixed in 1% osmium tetroxide solution and dehydrated with gradient ethanol, culminating in their embedding in resin. The ultrathin sections were produced using a microtome and stained with double-stained by 2% uranyl acetate and lead citrate. Images were obtained by the TEM (Hitachi, HT7800, Japan).

Mitochondrial membrane potential assay

KYSE70 cells (1.0×10^5) were seeded on 12-well plates and pretreated with different formulations. Then, the JC-1 probe (KeyGen Biotech) was added. The fluorescence images were obtained by an inverted microscope (Thermo Fisher).

Intracellular ROS detection

KYSE70 cells (1.0×10^5) were seeded on 12-well plates and pretreated with different formulations. Then, the

DCFH-DA probe (Beyotime) was added. After 30 min, the images were recorded by CLSM.

Examination of LPO in vitro

KYSE70 cells (1.0×10^5) were seeded on 12-well plates and pretreated with different formulations. Subsequently, cells were incubated with the $BODIPY^{581/591}$ probe (Thermo Fisher). Finally, the fluorescence images were recorded by CLSM.

Intracellular MDA content

KYSE70 cells (5.0×10^5) were seeded on 6-well plates and pretreated with different formulations. MDA content was assessed using a commercial assay kit (Solarbio).

Western blot assay

KYSE70 cells (1.0×10^6) were subjected to different treatments. Then, cells were lysed with RIPA buffer (Thermo Fisher) and collected. The concentration was quantified with a commercial BCA protein assay Kit (CWBio). Cellular proteins were separated via SDS-PAGE, followed by protein transfer to PVDF membranes at 4 °C for 2 h. Subsequently, PVDF membranes were blocked with 5% skim milk for 1.5 h and then incubated with primary antibodies, including anti-GPX4 antibody (Cell Signaling Technology, 52455 S, 1:1000) and anti-SLC7A11 antibody (Abcam, Ab175186, 1:2500) at 4 °C overnight. Afterward, the membranes were washed with TBST and incubated with the HRP-conjugated secondary antibody (Proteintech, SA00001-2; 1:5000) for another 2 h. Proteins were detected with an ECL assay kit (Epizyme) and imaged under a chemiluminescence imaging system (Bio-Rad, ChemiDoc XRS+, USA).

Ferroptosis PCR array

Gene expression profiles were analyzed using the human targets of ferroptosis PCR array (Woji Gene). Total RNA was extracted from the cells with different treatments using the TRIzol reagent. Then, RNA was subjected to cDNA synthesis using HiScript QRT SuperMix (Vazyme). qRT-PCR was performed using the 2×Taq Plus Master (Vazyme) and subsequently analyzed using the CFX connect system (Bio-Rad). Relative gene expression levels were calculated by the $2^{-\Delta\Delta Ct}$ method and were normalized to the expression of the internal control GAPDH.

Intracellular GSH content assay

KYSE70 cells (1.5×10^5) were subjected to different treatments. After 24 h, the cellular GSH content was assessed using the GSH assay kit (Nanjing Jiancheng).

Expression of CRT assay

KYSE70 cells (5.0×10^3) were subjected to different treatments in confocal dishes. After 24 h, the cells were treated with 4% PFA for fixation and 0.2% Triton X-100 for permeation. Next, the cells were blocked with a 5% BSA buffer. Subsequently, the cells were incubated with anti-CRT antibody (Servicebio, GB112134, 1:500) at 4 °C. Then, the cells were washed and incubated with Alexa Fluor™ 488 secondary antibody (Thermo Fisher, A-11008, 1:1000) for 1 h. Finally, the cells were treated with DAPI to stain the nucleus. The fluorescence images were recorded by CLSM.

HMGB1 and ATP secretion assay

KYSE70 cells (1.5×10^5) were subjected to different treatments. After 24 h, the expression of HMGB1 was assessed using the ELISA assay kit (Elabscience). The ATP concentrations were analyzed using a Microplate luminometer (GloMax Navigator) according to the ATP assay kit (Beyotime).

Animals assay

AKR and KYSE70 tumor models were established using C57BL/6 and BALB/c mice, weighing around 16 ~ 18 g and aged between 6 ~ 8 weeks. All mice were provided with humane care, and the experimental procedures adhered to the Guide for the Care and Use of Laboratory Animals, as approved by the Animal Care Committee of The First Affiliated Hospital of Henan University of Science and Technology (202203B111).

Hemolytic assay

Red blood cells (RBCs) were obtained from mice blood via centrifugation (2000 rpm, 10 min). Before usage, the obtained RBCs were dispersed ten times the volume of Saline. For the hemolysis test, DI water and saline solution served as positive and negative control respectively, and CS@Fc solution of various concentrations (25, 50, 75, 100 μg/mL) served as the experimental groups. After incubating at 37 °C for 2 h, the supernatants of all the samples were collected to measure their absorbance at 540 nm. The hemolysis percentage (HP) was calculated using the following formula:

$$\mathrm{HP} = \frac{A_S - A_{C(-)}}{A_{C(+)} - A_{C(-)}} \times 100\%$$

As, $A_{C(-)}$ and $A_{C(+)}$ represent the absorbance of the CS@Fc, saline, and DI water, respectively.

In vivo biodistribution

The mice were injected Free DiR (1 mg/kg) and CS@DiR (10 mg/kg) respectively. The fluorescence was monitored

at 0, 2, 4, 8, 12, 24, and 48 h postinjection in vivo imaging system (PerkinElmer, IVIS Lumina Series III, USA).

In vivo antitumor activity of CS@Fc

When tumors reached 100 mm^3, mice were randomly divided into seven groups ($n = 6$), including the Saline, Fc (2 mg/kg), CS (10 mg/kg), CS@Fc (10 mg/kg), CS + NIR, CS@Fc + NIR, and CS@Fc + NIR + GSH (5 mg/kg) groups. The body weight and the length and width of each tumor were recorded every 3 days. The tumor volume was calculated from measurements using the following formula: volume (mm^3) = length × $width^2$ / 2. After five treatments, the mice in each group were euthanatized to collect blood, tumors, and major organs. Tumor tissues were fixed with 4% PFA, embedded into paraffin, and sliced at 5 μm thickness for H&E staining, immunohistochemical assay and immunofluorescence analyses.

In vivo antitumor efficacy of combined CS@Fc and Anti-PD-1 therapy

C57BL/6 mice were subcutaneously inoculated with 1×10^6 AKR tumor cells in the right flank. Upon the tumor volume reaching approximately 80–100 mm^3, the mice were randomly allocated into four groups ($n = 6$): saline control group, Anti-PD-1 treatment group (15 mg/kg, administered via *i.p.* injection every 3 days), CS@Fc + NIR group (10 mg/kg, administered via insitu-injection every 3 days), and the combination treatment group receiving both CS@Fc + NIR and Anti-PD-1 therapy. At 8 h post-injection, the tumor sites in the CS@Fc + NIR and CS@Fc + NIR + Anti-PD-1 groups were subjected to irradiation with a 980 nm laser to maintain a temperature of 45 °C for 5 min. Tumor volume and body weight were monitored every 3 days. The length (L) and width (W) of the tumor were measured every 3 days using a digital caliper, and the tumor volume was calculated as $0.5 \times L \times W^2$. Mice were euthanized in accordance with animal care guidelines when the tumor volume reached approximately 2000 mm^3. Tumor samples were subsequently collected for further tumor immune microenvironment analysis.

Flow cytometry analysis

Tumor infiltrating lymph nodes were isolated from subcutaneous tumor-bearing mice subjected to various treatments. The tissues underwent enzymatic digestion with collagenase and subsequent filtration to obtain single-cell suspensions. DCs were stained using FITC-conjugated anti-mouse CD11c antibody and PE/Cy7-conjugated anti-mouse I-A/I-E antibody. Lymphocytes were stained with FITC-conjugated anti-mouse CD3 antibody, PerCP/Cy5.5-conjugated anti-mouse CD4 antibody, and APC-conjugated anti-mouse CD8a antibody. For functional CTLs staining, cell suspensions were restimulated with a Cell Activation Cocktail in the presence of Brefeldin A for 4 h. Subsequently, the restimulated lymphocytes were stained with FITC-conjugated anti-mouse CD3 antibody and APC conjugated anti-mouse CD8a antibody. Following surface staining, cells were fixed and permeabilized using a Fix/Perm solution, followed by re-staining with PE-conjugated anti-mouse IFN-γ antibody for intracellular cytokine analysis. For Treg cell staining, cells were first stained with PerCP/Cy5.5-conjugated anti-mouse CD4 antibody and APC-conjugated anti-mouse CD25 antibody. Following fixation and permeabilization with Fix/Perm solution, cells were restained with PE-conjugated anti-mouse Foxp3 antibody. Flow cytometric analysis was performed using a CytoFlex flow cytometry system.

Statistical analysis

All data are presented as mean ± SD and were analyzed using GraphPad Prism 8 and Origin 2023 software. Error bars shown represent the standard error derived from three independent measurements. Normality tests were performed in all experiments. We performed significance analyses by Student's *t*-test, and one-way analysis of variance (ANOVA) results with the Tukey test. $^*P < 0.05$, $^{**}P < 0.01$, and $^{***}P < 0.001$ were considered statistically significant.

Supplementary Information

The online version contains supplementary material available at https://doi.org/10.1186/s12951-025-03434-7.

Supplementary Material 1

Author contributions

Linlin Shi and Ying Yu contributed equally to this work. Conceptualization: Shegan Gao, Linlin Shi, Haoyan Cheng; Methodology: Ying Yu, Jiayi Li, Beng Ma; Investigation: Ying Yu, Jiayi Li, Xiaoman Zhang, Zhifeng Qu, Pan Chen, Fengqi Zhang, Ke Liu, Pingjuan Yang; Writing (original draft): Ying Yu, Beng Ma, Linlin Shi, Haoyan Cheng; Writing (review & editing): Shegan Gao, Linlin Shi, Haoyan Cheng.

Funding

This work was supported by the National Natural Science Foundation of China (82302966), the Leading Academic Discipline Project of Henan Provincial Health Commission, the Physician-Scientist Training Project in Henan Province (S20240247), the Central Plains Outstanding Young Leading Talents Program for Scientific and Technological Innovation, the National Clinical Key Specialty Construction Foundation of China (ZLKFJJ20230401) and the Joint Fund of the Major Science and Technology Projects in Henan Province (235200810002). This work was also sponsored by the Natural Science Foundation of Henan (252300421104).

Data availability

No datasets were generated or analysed during the current study.

Declarations

Ethics approval and consent to participate

All mice received the humane care and the experimental protocols were carried out in accordance with the Guide for the Care and Use of Laboratory

Animals, as approved by the Animal Care Committee of The First Affiliated Hospital of Henan University of Science and Technology (202203B111).

Consent for publication
All authors agree to submit the manuscript for publication.

Competing interests
The authors declare no competing interests.

Author details
[1]Henan Key Laboratory of Microbiome and Esophageal Cancer Prevention and Treatment, State Key Laboratory of Esophageal Cancer Prevention & Treatment, Henan Key Laboratory of Cancer Epigenetics, The First Affiliated Hospital, College of Clinical Medicine, Henan University of Science and Technology, Luoyang 471003, China
[2]Institute of Organoid on Chip and Drug Translation Research, Henan Academy of Sciences, Zhengzhou 450003, China
[3]School of Materials Science and Engineering, The First Affiliated Hospital, College of Clinical Medicine, Henan University of Science and Technology, Luoyang 471023, China

Received: 14 November 2024 / Accepted: 1 May 2025
Published online: 17 May 2025

References

1. Liu C-Q, Ma Y-L, Qin Q, Wang P-H, Luo Y, Xu P-F, Cui Y. Epidemiology of esophageal cancer in 2020 and projections to 2030 and 2040. Thorac Cancer. 2023;14:3–11.
2. Shah MA, Hofstetter WL. Kennedy, N. N.ll, immunotherapy in patients with locally advanced esophageal carcinoma: ASCO treatment of locally advanced esophageal carcinoma guideline rapid recommendation update. J Clin Oncol. 2021;39:3182–4.
3. Liang H, Fan JH, Qiao YL. Epidemiology, etiology, and prevention of esophageal squamous cell carcinoma in China. Cancer Biol Med. 2017;14:33–41.
4. Liu J, Gao J, Zhang A, Guo Y, Fan S, He Y, Yang K, Wang J, Cui D, Cheng Y. Carbon nanocage-based nanozyme as an endogenous H_2O_2-activated oxygenerator for real-time bimodal imaging and enhanced phototherapy of esophageal cancer. Nanoscale. 2020;12:21674–86.
5. Overchuk M, Weersink RA, Wilson BC, Zheng G. Photodynamic and photothermal therapies: synergy opportunities for nanomedicine. ACS Nano. 2023;17:7979–8003.
6. Liu B, Li C, Cheng Z, Hou Z, Huang S, Lin J. Functional nanomaterials for near-infrared-triggered cancer therapy. Biomater Sci. 2016;4:890–909.
7. Chen G, Roy I, Yang C, Prasad PN. Nanochemistry and nanomedicine for Nanoparticle-based diagnostics and therapy. Chem Rev. 2016;116:2826–85.
8. Ivanchenko M, Evangelista AJ, Jing H. Palladium-rich plasmonic nanorattles with enhanced LSPRs via successive galvanic replacement mediated by co-reduction. RSC Adv. 2021;11:40112–9.
9. Huang X, Lu Y, Guo M, Du S, Han N. Recent strategies for nano-based PTT combined with immunotherapy: from a biomaterial point of view. Theranostics. 2021;11:7546–69.
10. Yi X, Duan Q-Y, Wu F-G. Low-temperature photothermal therapy: strategies and applications, Research. 2021; 2021: 9816594.
11. Xie S, Sun W, Zhang C, Dong B, Yang J, Hou M, Xiong L, Cai B, Liu X, Xue W. Metabolic control by heat stress determining cell fate to ferroptosis for effective Cancer therapy. ACS Nano. 2021;15:7179–94.
12. Tian B, Wang C, Zhang S, Feng L, Liu Z. Photothermally enhanced photodynamic therapy delivered by nano-graphene oxide. ACS Nano. 2011;5:7000–9.
13. Huang X, Wu J, He M, Hou X, Wang Y, Cai X, Xin H, Gao F, Chen Y. Combined cancer chemo-photodynamic and photothermal therapy based on ICG/PDA/TPZ-loaded nanoparticles. Mol Pharm. 2019;16:2172–83.
14. Huang L, Li Y, Du Y, Zhang Y, Wang X, Ding Y, Yang X, Meng F, Tu J, Luo L, Sun C. Mild photothermal therapy potentiates anti-PD-L1 treatment for immunologically cold tumors via an all-in-one and all-in-control strategy. Nat Commun. 2019;10:4871.
15. Stockwell BR. Ferroptosis turns 10: emerging mechanisms, physiological functions, and therapeutic applications. Cell. 2022;185:2401–21.
16. Su Y, Zhao B, Zhou L, Zhang Z, Shen Y, Lv H, AlQudsy LHH, Shang P. Ferroptosis, a novel pharmacological mechanism of anti-cancer drugs. Cancer Lett. 2020;483:127–36.
17. Hassannia B, Vandenabeele P, Vanden Berghe T. Targeting ferroptosis to iron out cancer. Cancer Cell. 2019;35:830–49.
18. He S, Jiang Y, Li J, Pu K. Semiconducting polycomplex nanoparticles for photothermal ferrotherapy of cancer. Angew Chem Int Ed. 2023;14:10633–8.
19. Duan Y, Yang H, Gao J, Wei D, Zhang Y, Wang J, Zhang X, Zhang J, Ge K, Wu X, Chang J. Immune modulator and low-temperature PTT-induced synergistic immunotherapy for cancer treatment. ACS Appl Bio Mater. 2021;4:1524–35.
20. Shi L, Liu Y, Li M, Luo Z. Emerging roles of ferroptosis in the tumor immune landscape: from danger signals to anti-tumor immunity. FEBS J. 2020;289:3655–65.
21. Xie D, Wang Q, Wu G. Research progress in inducing immunogenic cell death of tumor cells. Front Immuno. 2020;13:1017400.
22. Zheng H, Jiang J, Xu S, Liu W, Xie Q, Cai X, Zhang J, Liu S, Li R. Nanoparticle-induced ferroptosis: detection methods, mechanisms and applications. Nanoscale. 2021;13:2266–85.
23. Lampe RH, Coale TH, Forsch KO, Jabre LJ, Kekuewa S, Bertrand EM, Horák A, Oborník M, Rabines AJ, Rowland E, Zheng H, Andersson AJ, Barbeau KA, Allen AE. Short-term acidification promotes diverse iron acquisition and conservation mechanisms in upwelling-associated phytoplankton. Nat Commun. 2023;14:7215.
24. Li Y, Wei X, Tao F, Deng C, Lv C, Chen C, Cheng Y. The potential application of nanomaterials for ferroptosis-based cancer therapy. Biomed Mater. 2021;16:042013.
25. Zhu C, Huo D, Chen Q, Xue J, Shen S, Xia Y. A eutectic mixture of natural fatty acids can serve as the gating material for near-infrared-triggered drug release. Adv Mater. 2017;29:1703702.
26. Cheng H, Huo D, Zhu C, Shen S, Wang W, Li H, Zhu Z, Xia Y. Combination cancer treatment through photothermally controlled release of selenous acid from gold nanocages. Biomaterials. 2018;178:517–26.
27. Liu Y, Chen J, He Z, Luo H, Liu X, Sun Y, Ge D, Liu X, Shi W. Ferrocene-liposome-PEG: a robust ·OH/lipid peroxide nano-converter for inducing tumor ferroptosis. Biomater Sci. 2023;11:542–53.
28. Li J, Zong Q, Liu Y, Xiao X, Zhou J, Zhao Z, Yuan Y. Self-catalyzed tumor ferroptosis based on ferrocene conjugated reactive oxygen species generation and a responsive polymer. Chem Commun. 2022;58:3294–7.
29. Li K, Xu K, He Y, Yang Y, Tan M, Mao Y, Zou Y, Feng Q, Luo Z, Cai K. Oxygen self-generating nanoreactor mediated ferroptosis activation and immunotherapy in triple- nbegative breast Cancer. ACS Nano. 2023;17:4667–87.
30. Zhang Z, Xue H, Xiong Y, Geng Y, Panayi AC, Knoedler S, Dai G, Shahbazi MA, Mi B, Liu G. Copper incorporated biomaterial-based technologies for multifunctional wound repair. Theranostics. 2024;14:547–70.
31. Cheng H, Xia W, Zhao Z, Wang W, Song K, Li H, Cheng C, Hu H. Tailoring Core@shell structure of $Cu_{2-x}Se$@PDAs for synergistic solar-driven water evaporation. J Mater Sci. 2022;57:11725–34.
32. Chen H, Shao L, Ming T, Sun Z, Zhao C, Yang B, Wang J. Understanding the photothermal conversion efficiency of gold nanocrystals. Small. 2010;6:2272–80.
33. Cheng D, Ji Y, Wang B, Wang Y, Tang Y, Fu Y, Xu Y, Qian X, Zhu W. Dual-responsive nanohybrid based on degradable silica-coated gold nanorods for triple-combination therapy for breast cancer. Acta Biomater. 2021;128:435–46.
34. Grubwieser P, Brigo N, Seifert M, Grander M, Theurl I, Nairz M, Weiss G, Pfeifhofer-Obermair C. Quantification of macrophage cellular ferrous iron ($Fe^{(2+)}$) content using a highly specific fluorescent probe in a plate reader. Bio Protoc. 2024;14:e4929.
35. Dixon SJ, Lemberg KM, Lamprecht MR, Skouta R, Zaitsev EM, Gleason CE, Patel DN, Bauer AJ, Cantley AM, Yang WS, Morrison B, Stockwell BR. Ferroptosis: an iron-dependent form of nonapoptotic cell death. Cell. 2012;149:1060–72.
36. Gan B. Mitochondrial regulation of ferroptosis. J Cell Biol. 2021;220:e202105043.
37. Wang T, Zhang H, Qiu W, Han Y, Liu H, Li Z. Biomimetic nanoparticles directly remodel immunosuppressive microenvironment for boosting glioblastoma immunotherapy. Bioact Mater. 2022;16:418–32.
38. Qin W, Huang J, Yang C, Yue Q, Chen S, Wang M, Gao S, Zhou X, Yang X, Zhang Y. Protease-Activatable nanozyme with photoacoustic and Tumor-Enhanced magnetic resonance imaging for photothermal ferroptosis Cancer therapy. Adv Funct Mater. 2023;33:2209748.
39. Maeda H, Wu J, Sawa T, Matsumura Y, Hori K. Tumor vascular permeability and the EPR effect in macromolecular therapeutics: a review. J Control Release. 2000;65:271–84.

40. Shi Y, van der Meel R, Chen X, Lammers T. The EPR effect and beyond: strategies to improve tumor targeting and cancer nanomedicine treatment efficacy. Theranostics. 2010;10:7921–4.
41. Yang Z, Gao D, Zhao J, Yang G, Guo M, Wang Y, Ren X, Kim JS, Jin L, Tian Z, Zhang X. Thermal immuno-nanomedicine in cancer. Nat Rev Clin Oncol. 2023;20:116–34.
42. Chen B, Huang R, Zeng W, Wang W, Min Y. Nanocodelivery of an NIR photothermal agent and an acid-responsive TLR7 agonist prodrug to enhance cancer photothermal immunotherapy and the abscopal effect. Biomaterials. 2024;305:122434.
43. Ni W, Wu J, Fang H, Feng Y, Hu Y, Lin L, Chen J, Chen F, Tian H. Photothermal-Chemotherapy enhancing tumor immunotherapy by multifunctional Metal–Organic framework based drug delivery system. Nano Lett. 2021;21:7796–805.
44. Chen M, Li J, Shu G, Shen L, Qiao E, Zhang N, Fang S, Chen X, Zhao Z, Tu J, Song J, Du Y, Ji J. Homogenous multifunctional microspheres induce ferroptosis to promote the anti-hepatocarcinoma effect of chemoembolization. J Nanobiotechnol. 2022;20:179.
45. Tyurina YY, Kapralov AA, Tyurin VA, Shurin G, Amoscato AA, Rajasundaram D, Tian H, Bunimovich YL, Nefedova Y, Herrick WG, Parchment RE, Doroshow JH, Bayir H, Srivastava AK, Kagan VE. Redox phospholipidomics discovers pro-ferroptotic death signals in A375 melanoma cells in vitro and in vivo. Redox Biol. 2023;61:102650.
46. Wang D, Qiu G, Zhu X, Wang Q, Zhu C, Fang C, Liu J, Zhang K, Liu Y. Macrophage-inherited exosome excise tumor immunosuppression to expedite immune-activated ferroptosis. J Immunother Cancer. 2023;11:e006516.
47. Xiao Q, Zheng X, Bu W, Ge W, Zhang S, Chen F, Xing H, Ren Q, Fan W, Zhao K, Hua Y, Shi J. A core/satellite multifunctional nanotheranostic for in vivo imaging and tumor eradication by radiation/photothermal synergistic therapy. J Am Chem Soc. 2013;135:13041–8.
48. Xie J, Gong L, Zhu S, Yong Y, Gu Z, Zhao Y. Emerging strategies of nanomaterial-mediated tumor radiosensitization. Adv Mater. 2019;31:1802244.
49. Shen Z, Xia J, Ma Q, Zhu W, Gao Z, Han S, Liang Y, Cao J, Sun Y. Tumor Microenvironment-triggered nanosystems as dual-relief tumor hypoxia immunomodulators for enhanced phototherapy. Theranostics. 2020;10:9132–52.

Publisher's note